

Left-invariant Evolutions of Wavelet Transforms on the Similitude Group

Upanshu Sharma and Remco Duits

*Upanshu Sharma, Department of Mathematics and Computer Science, Eindhoven University of Technology, 5600 MB Eindhoven, The Netherlands,
u.sharma@tue.nl*

*Remco Duits, Department of Mathematics and Computer Science & Department of Biomedical Engineering, Eindhoven University of Technology, 5600 MB Eindhoven, The Netherlands,
r.duits@tue.nl*

Abstract

Enhancement of multiple-scale elongated structures in noisy image data is relevant for many biomedical applications but commonly used PDE-based enhancement techniques often fail at crossings in an image. To get an overview of how an image is composed of local multiple-scale elongated structures we construct a continuous wavelet transform on the similitude group, $SIM(2)$. Our unitary transform maps the space of images onto a reproducing kernel space defined on $SIM(2)$, allowing us to robustly relate Euclidean (and scaling) invariant operators on images to left-invariant operators on the corresponding continuous wavelet transform. Rather than often used wavelet (soft-)thresholding techniques, we employ the group structure in the wavelet domain to arrive at left-invariant evolutions and flows (diffusion), for contextual crossing preserving enhancement of multiple scale elongated structures in noisy images. We present experiments that display benefits of our work compared to recent PDE techniques acting directly on the images and to our previous work on left-invariant diffusions on Coherent state transforms defined on Euclidean motion group.

Keywords: Continuous wavelet transform, Left-invariant vector fields, Similitude group, Evolution equations, Diffusions on Lie groups, Medical imaging

1. Introduction

Elongated structures in the human body such as fibres and blood vessels often require analysis for diagnostic purposes. A wide variety of medical imaging techniques such as magnetic resonance imaging (MRI), microscopy, X-ray fluoroscopy, fundus imaging etc. exist to achieve this. Many (bio)medical questions related to such images require detection and tracking of the elongated structures present therein. Due to the desire to reduce acquisition time and radiation dosage the acquired medical images are often noisy, of low contrast and suffer from occlusions and incomplete data. Furthermore multiple-scale elongated structures exhibit crossings and bifurcations which is a notorious problem in (medical) imaging. Hence crossing-preserving enhancement of these structures is an important preprocessing step for subsequent detection.

In recent years PDE based techniques have gained popularity in the field of image processing. Due to well posed mathematical results these techniques lend themselves to stable algorithms and also allow mathematical and geometrical interpretation of classical methods such as Gaussian and morphological filtering, dilation or erosion etc. on \mathbb{R}^d . These techniques typically regard the original image, $f \in \mathbb{R}^2 \rightarrow \mathbb{R}$, as an initial state of a parabolic (diffusion like) evolution process yielding filtered versions, $u_f : \mathbb{R}^2 \times \mathbb{R}^+ \rightarrow \mathbb{R}$. Here u_f is called the scale space representation of image f . The domain of u_f is scale space $\mathbb{R}^2 \times \mathbb{R}^+$. A typical scale space evolution is of the form

$$\begin{cases} \partial_s u_f(\mathbf{x}, s) &= \nabla_{\mathbf{x}} \cdot (C(u_f(\cdot, s))(\mathbf{x}) \nabla_{\mathbf{x}} u_f)(\mathbf{x}, s) \\ u_f(\mathbf{x}, 0) &= f(\mathbf{x}), \end{cases} \quad (1)$$

where $C(u_f(\cdot, s))(\mathbf{x})$ models the diffusivity depending on the differential structure at $(\mathbf{x}, s, u_f(\mathbf{x}, s)) \in \mathbb{R}^d \times \mathbb{R}^+ \times \mathbb{R}$. For $C = 1$, Eq.(1) is the usual linear heat equation. The corresponding evolution is known in image processing as a Gaussian Scale Space [1, 2, 3, 4]. In their seminal paper [5], Perona and Malik proposed nonlinear filters to bridge scale space and restoration ideas. Based on the observation that diffusion should not occur when the (local) gradient value is large (to avoid blurring the edges), they pointed out that nonlinear adaptive isotropic diffusion is achieved by replacing $C = 1$ by $C(u_f(\cdot, s))(\mathbf{x}) = c(\|\nabla_{\mathbf{x}} u_f(\mathbf{x}, s)\|)$, where $c : \mathbb{R}^+ \rightarrow \mathbb{R}^+$ is some smooth strictly decreasing positive function vanishing at infinity. An improvement of the Perona-Malik scheme is the ‘‘coherence-enhancing diffusion’’ (CED) introduced by Weickert [6] which additionally uses the direction of the gradient $\nabla_{\mathbf{x}} u_f$ leading to diffusion constant c being replaced by a nonlinear matrix.

However these methods often fail in image analysis applications with crossing or bifurcating curves as the direction of gradient at these structures is ill-defined, see [7] for more details. Scharr et al. in [8] present techniques which effectively deal with the particular case of X-junctions by relying on the 2-nd order jet of Gaussian derivatives in the image domain. Passing through higher order jets of Gaussian derivatives and induced Euclidean invariant differential operators does not allow one to generically deal with complex crossings and/or bifurcating structures. Instead we need gauge frames in higher dimensional Lie groups to deal with this issue. According to the terminology used in [9, Section 3.3.3] a gauge frame is a local coordinate system aligned/gauged with locally present (elongated) structures in an image. Differentiating w.r.t. such coordinates provides intrinsically natural derivatives as opposed to differentiating w.r.t. (artificially imposed) global coordinates. At salient locations in the image, where multiple scale elongated structures cross, one needs multiple gauge frames. Therefore instead of gauge frames per position, $x \in \mathbb{R}^2$ in a (grey-scale) image $f : \mathbb{R}^2 \rightarrow \mathbb{R}$, we attach gauge frames to each Lie group element,

$$g = (x, t) \in G = \mathbb{R}^2 \rtimes T.$$

in a Coherent state (CS) transform $\mathcal{W}_{\psi} f : G \rightarrow \mathbb{C}$ of an image $f : \mathbb{R}^2 \rightarrow \mathbb{R}$. In this article we mainly consider $(G = SE(2), T = SO(2))$ and $(G = SIM(2), T = \mathbb{R}^+ \times SO(2))$, where (multiple scale) elongated structures are manifestly disentangled via the transform, allowing for a crossing preserving flow (steered by gauge frames). In medical image processing $\mathcal{W}_{\psi} f$ for $G = SE(2)$ is also referred to as an orientation score as it provides a score of how an image is decomposed out of local (possibly crossing) orientations.

1.1. Why extend to the SIM(2) group?

In this paper we wish to extend the aforementioned framework to the case of the similitude group (group of planar translations, rotations and scaling), for the following reasons:

- Gauge frames based on Gaussian derivatives are usually aligned with a *single* Gaussian gradient direction, which is unstable in the vicinity of complex structures such as crossings and bifurcations. At these structures one needs multiple spatial frames per position. Therefore following the general idea of Scale spaces on groups which are a semidirect product of group of translations with other Lie groups [10, 11, 12, 13], a natural next step would be to extend the domain of images to the Lie group $SIM(2) = \mathbb{R}^2 \rtimes (\mathbb{R}^+ \times SO(2))$ in order to have well posed gauge frames at crossing structures (adapted to multiple orientations and scales that are locally present).
- In the primary visual cortex both multiple scales and orientations are encoded per position. It is generally believed that receptive field profiles in neurophysiological experiments can be modelled by Gaussian derivatives [14, 15, 16, 17] and this provides a biological motivation to incorporate scales.
- Elongated (possibly crossing) structures often exhibit multiple scales. Earlier work by one of the authors [18, 7] proposes generic crossing preserving flows via CS transform (without explicit multiple scale decomposition). However, this approach treats all scales in the same way. As a result these flows do not always adequately deal with images containing elongated structures with strongly varying widths (scales). Therefore we must encode and process multiple scales in the transform.

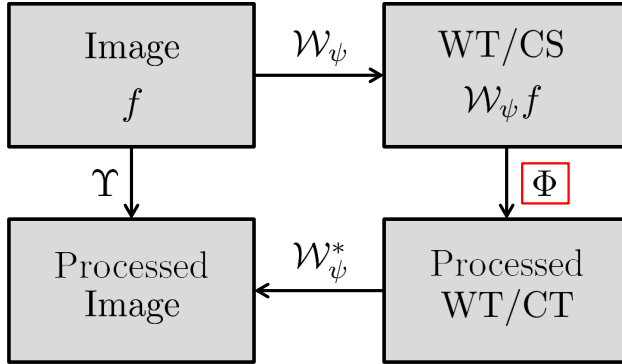


Figure 1: A schematic view on processing images $f : \mathbb{R}^2 \rightarrow \mathbb{R}$ via WT/CS transform $\mathcal{W}_\psi f : G \rightarrow \mathbb{C}$ defined on Lie group $G = \mathbb{R}^2 \rtimes T$. Design of well posed transform \mathcal{W}_ψ and of appropriate operators Φ is the main objective of this article. Note that $\Upsilon = \mathcal{W}_\psi^* \circ \Phi \circ \mathcal{W}_\psi$, i.e. spatial processes are realized via invertible transforms akin to cortical columns in the visual brain [34].

Our framework involves the construction of an appropriate continuous wavelet transform (WT) of an image using the similitude group. This approach is related to that of directional wavelets [19, 20, 21, 22, 23] and curvelets [24, 25, 26, 27]. In particular the recent popular approach of shearlets [28, 29, 30, 31] also falls in the category of continuous wavelet transform but uses the shearlet group which includes the shearing, translation and scaling group. The main aim of this article is to construct rotation and translation invariant diffusion type flows on the wavelet transformed image. Although highly useful, the shearlet group (which is related to the Similitude group by nilpotent approximations, see [32, Appendix E]) is not very suited for such exact rotation and translation covariant processing because of its group structure.

1.2. Our main results

There are two main motivating questions (see Figure 1) for the work presented in this article.

1. Can we design a wavelet transform, which is a complex-valued function on Lie group $SIM(2)$, combining the strengths of directional wavelets [19, 20, 21], curvelets [24, 25, 26, 27] in a way that allows for accurate and efficient implementation of subsequent contextual-enhancement operators?
2. Can we construct contextual flows in the wavelet domain, in order to ensure that only the wavelet coefficients that are coherent (from both probabilistic and group theoretical perspective, [33]) with the surrounding coefficients become dominant?

Our answer to both these questions is affirmative. In the first part we follow the general approach by Grossmann, Morlet and Paul in [35], Ali in [33] and Führ in [36] and provide a short review of general results in the context of our case of interest. In practice there are upper/lower bounds on scaling and so in Theorem 4 we provide stability analysis and condition number of a modified continuous wavelet transform on $SIM(2)$ which can be used for practical applications. The crucial point in our design is that we rely on explicit B-spline decomposition along log-polar type of coordinates in the Fourier domain. These are the canonical coordinates of the second type for $SIM(2)$, which are required for accurate left-invariant processing on the CS transformed images. Figure 2 depicts the use of this wavelet transform in practice.

The latter and main part of this article is dedicated to answering the second question. Theorem 8 shows that only left-invariant operators on the transformed image correspond to Euclidean (and scaling) invariant operators on images. Therefore, in this article we restrict ourselves to left-invariant PDE evolutions on $SIM(2)$. Theorem 10 provides a stochastic connection to our left-invariant flows in the wavelet domain. These flows are forward Kolmogorov equations corresponding to stochastic processes for multiple-scale contour enhancement on $SIM(2)$. Using the general theory of coercive operators on Lie groups, in Eq.(46) Gaussian estimates for the Green's function of linear diffusion on $SIM(2)$ are derived. In Eq.(49) we present nonlinear left-invariant adaptive diffusions on the image of a wavelet transform. Finally, we present experiments to validate the clear practical advantages of our approach over existing PDE-based techniques and include comparisons to other denoising methods.

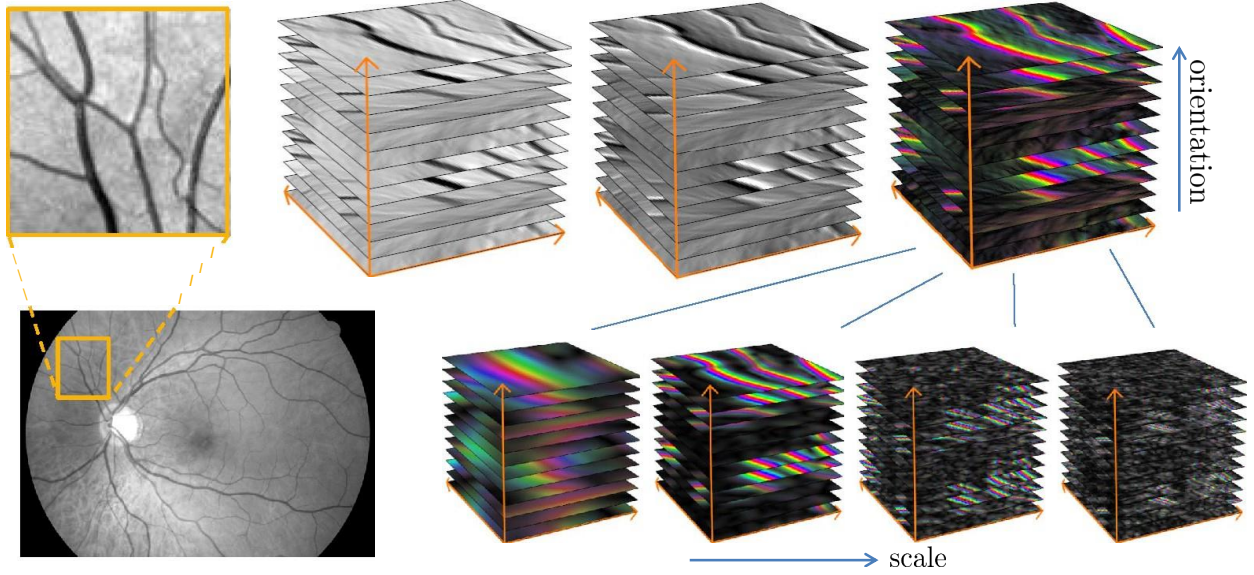


Figure 2: Top row: original image, the real-part of the CS transform on $SE(2)$ group reflects the centerlines, the imaginary part the edges of the bloodvessels, the combination (color represents phase direction and intensity represents the absolute value). Bottom row: visualizations of CW Transform on $SIM(2)$ group that allow us to include scale adaptation in our enhancement and detection.

1.3. Coherent state transform on $SE(2)$

Based on the early work by Ali, Antoine and Gazeau [23] and Kalitzin [37], Duits et al. [18, 13] introduced the framework of CS transforms on $SE(2)$ in medical imaging to effectively handle the problem of generic crossing curves in the context of bio-medical applications. Now we briefly summarize the ideas developed in [18, 13]. The $2D$ -Euclidean motion group (i.e. the group of planar rotations and translations) $SE(2)$ is defined as $SE(2) = \mathbb{R}^2 \rtimes SO(2)$. A CS transform, $U_f : SE(2) \rightarrow \mathbb{C}$ of an image $f : \mathbb{R}^2 \rightarrow \mathbb{R}$ is obtained by means of an anisotropic convolution kernel $\check{\psi} : \mathbb{R}^2 \rightarrow \mathbb{C}$ via

$$U_f(g) = \int_{\mathbb{R}^2} \overline{\check{\psi}(\mathbf{R}_\theta^{-1}(\mathbf{y} - \mathbf{x}))} f(\mathbf{y}) d\mathbf{y}, \quad g = (\mathbf{x}, \theta) \in SE(2),$$

where $\psi(-\mathbf{x}) = \check{\psi}(\mathbf{x})$ and $\mathbf{R}_\theta \in SO(2)$ is the 2D counter-clockwise rotation by angle $\theta \in [0, 2\pi)$. Assuming $\psi \in \mathbb{L}_2(\mathbb{R}^2)$, the transform \mathcal{W}_ψ which maps images $f \in \mathbb{L}_2(\mathbb{R}^2)$ can be rewritten as

$$U_f(g) = (\mathcal{W}_\psi f)(g) = (\mathcal{U}_g \psi, f)_{\mathbb{L}_2(\mathbb{R}^2)},$$

where $g \mapsto \mathcal{U}_g$ is a unitary (group-)representation of the Euclidean motion group $SE(2)$ into $\mathbb{L}_2(\mathbb{R}^2)$ given by $\mathcal{U}_g f(\mathbf{y}) = f(\mathbf{R}_\theta^{-1}(\mathbf{y} - \mathbf{x}))$ for all $g = (\mathbf{x}, \mathbf{R}_\theta) \in SE(2)$ and for all $f \in \mathbb{L}_2(\mathbb{R}^2)$. It is constructed by means of an admissible vector $\psi \in \mathbb{L}(\mathbb{R}^2)$ such that \mathcal{W}_ψ is unitary onto the unique reproducing kernel Hilbert space $\mathbb{C}_K^{SE(2)}$ of functions on $SE(2)$ with reproducing kernel $K(g, h) = (\mathcal{U}_g \psi, \mathcal{U}_h \psi)$, which is a closed vector subspace of $\mathbb{L}_2(SE(2))$. This leads to the essential Plancherel formula (see [33, 36])

$$\|\mathcal{W}_\psi f\|_{\mathbb{C}_K^{SE(2)}}^2 = \int_{\mathbb{R}^2} \int_0^{2\pi} |(\mathcal{F}\mathcal{W}_\psi f)(\boldsymbol{\omega}, \theta)|^2 \frac{1}{M_\psi(\boldsymbol{\omega})} d\boldsymbol{\omega} d\theta = \int_{\mathbb{R}^2} |(\mathcal{F}f)(\boldsymbol{\omega})|^2 d\boldsymbol{\omega} = \|f\|_{\mathbb{L}_2(\mathbb{R}^2)}^2,$$

where $M_\psi \in C(\mathbb{R}^2, \mathbb{R})$ is given by $M_\psi(\boldsymbol{\omega}) = \int_0^{2\pi} |\mathcal{F}\psi(\mathbf{R}_\theta^T \boldsymbol{\omega})|^2 d\theta$ and \mathcal{F} denotes the Fourier transform. For examples of wavelets ψ and details on fast approximative reconstruction by integration over angles only, see [13]. For details on image processing via CS transform on $SE(2)$, see [38, 7, 39, 40]. In Figure 2 (top row) we depict a practical example of this transform.

1.4. Structure of the article

This article is structured as follows.

- **(Section 2) Unitary CS transform on images:** Stability of the CS transform is discussed followed by an explicit construction of so called proper wavelets that allow for both a stable (re)construction of the transformed image and accurate implementation of subsequent left-invariant flows.
- **(Section 3) Operators on transformed image:** Employing the group structure in the wavelet domain a general framework for operators on the transformed image involving left-invariant evolutions is discussed. These operators are interpreted in a differential geometric (and probabilistic) setting to provide a strong intuitive rationale for their choice.
- **(Section 4) Left-invariant diffusions:** Gaussian estimates for the Green's function of linear diffusion on $SIM(2)$ are derived followed by a discussion of non-linear adaptive diffusion.
- **(Section 5) Practical results:** In this section we present experiments that show the advantages of adaptive non-linear diffusion on CW transformed images in comparison to PDE techniques and we include comparisons with other denoising techniques.

2. Unitary operators between images and transforms

In this section we present a quick overview of abstract coherent state transforms from a Hilbert space to a functional Hilbert space and thereby arrive at a continuous wavelet transform in our case of interest, the $SIM(2)$ group. This is followed by quantifying the stability of this transform in a sense which will be made precise. We end the section by explicitly constructing so called proper wavelets which would allow us to create appropriate PDE flows in the subsequent sections. The continuous wavelet transform constructed by unitary irreducible representations of locally compact groups was first formulated by Grossman et al. [35]. Given a Hilbert space H and a unitary irreducible representation $g \mapsto \mathcal{U}_g$ of any locally compact group G in H , a nonzero vector $\psi \in H$ is called admissible if

$$C_\psi := \int_G \frac{|\langle \mathcal{U}_g \psi, \psi \rangle|^2}{(\psi, \psi)_H} d\mu_G(g) < \infty, \quad (2)$$

where μ_G denotes the left-invariant Haar measure. Given an admissible vector ψ and a unitary representation of a locally compact group G in H , the CS transform $\widetilde{\mathcal{W}}_\psi : H \rightarrow \mathbb{L}_2(G)$ is given by $(\widetilde{\mathcal{W}}_\psi[f])(g) = \langle \mathcal{U}_g \psi, f \rangle_H$. It is well known in mathematical physics [33], that $\widetilde{\mathcal{W}}_\psi$ is an isometric transform onto a closed reproducing kernel space \mathbb{C}_K^G with $K_\psi(g, g') = \frac{1}{C_\psi} \langle \mathcal{U}_g \psi, \mathcal{U}_{g'} \psi \rangle_H$ as an \mathbb{L}_2 -subspace. Note that we distinguish between the isometric wavelet transform $\widetilde{\mathcal{W}}_\psi : \mathbb{L}_2(\mathbb{R}^2) \rightarrow \mathbb{L}_2(G)$ and the unitary wavelet transform $\mathcal{W}_\psi : \mathbb{L}_2(\mathbb{R}^2) \rightarrow \mathbb{C}_K^G$ since the orthogonal projection onto \mathbb{C}_K^G is given by $\mathbb{P}_\psi = \widetilde{\mathcal{W}}_\psi \widetilde{\mathcal{W}}_\psi^*$ whereas $\mathcal{W}_\psi \mathcal{W}_\psi^* = I$.

2.1. Construction of a Unitary Map from H to \mathbb{C}_K^G

When G is a locally compact group the norm on \mathbb{C}_K^G has a simpler explicit form compared to usual description, see [13, Ch:7.2] and [41, Lemma 1.7]. One can give an explicit characterization of \mathbb{C}_K^G , in the case $G = \mathbb{R}^d \rtimes_\varphi T$, with T a linear algebraic group (for definition see [42]), $\varphi : T \rightarrow \text{Aut}(\mathbb{R}^d)$ is a homomorphism, \mathcal{U} the left-regular action of G onto $H = \mathbb{L}_2(\mathbb{R}^2)$ and thereby formulate a reconstruction theorem for Lie groups which are semi-direct products of translations with other Lie groups. Here, we drop the formal requirement of \mathcal{U} being square-integrable and ψ being admissible in the sense of (2). The reason being that it is not strictly needed for a lot of cases, such as $G = SE(d)$ and its left-regular action on $\mathbb{L}_2(\mathbb{R}^d)$ where general unitarity results for \mathcal{W}_ψ are obtained. For instance, such unitarity results are directly obtained via the Plancherel theorem on $SE(2)$ [39][App. A], where none of the irreducible representations with non-zero dual measures in the decomposition are square integrable. Finally, we note that natural extensions to distributional wavelet

transforms allow explicit operator closures that do become \mathbb{L}_2 -isometries [43][App. B], but the use of such distribution techniques is beyond the scope of this article.

We call $\psi \in \mathbb{L}_2(\mathbb{R}^d)$ an admissible vector if

$$0 < M_\psi(\omega) := (2\pi) \int_T \left| \frac{\mathcal{F}[\mathcal{R}_t \psi(\omega)]}{\sqrt{\det(\varphi(t))}} \right|^2 d\mu_T(t) < \infty \text{ for almost every } \omega \in \Omega, \quad (3)$$

with $\Omega = \{\omega \in \mathbb{R}^d \mid \text{Stab}(\omega) \text{ is compact}\}$ and $\text{Stab}(\omega) = \{t \in T \mid (\phi(t))^T \omega = \omega\}$, where \mathcal{R}_t for each $t \in T$ for any $f \in \mathbb{L}_2(\mathbb{R}^d)$ is defined as

$$\mathcal{R}_t f(x) = \frac{1}{\sqrt{\det(\varphi(t))}} f((\varphi(t)^{-1})x).$$

For an admissible vector $\psi \in H$, the span of $V_\psi = \{\mathcal{U}_g \psi \mid g \in G\}$, is dense in H . Further the corresponding CS transform $\mathcal{W}_\psi : H \rightarrow \mathbb{C}_K^G$ is unitary. This follows from general results in [36, Ch.5].

Theorem 1. *Let $G = \mathbb{R}^d \rtimes_\varphi T$ and ψ be an admissible vector in the sense that (3) is satisfied. Then $\mathcal{T}_{M_\psi} \Phi \in \mathbb{L}_2(G, d\mu_G(g))$ for all $\Phi \in \mathbb{C}_K^G$, where we define*

$$[\mathcal{T}_{M_\psi}[\Phi]](\mathbf{b}, t) := \mathcal{F}^{-1} \left[\omega \mapsto (2\pi)^{-d/4} M_\psi^{-1/2}(\omega) \mathcal{F}[\Phi(\cdot, t)](\omega) \right](\mathbf{b}).$$

Therefore $(\cdot, \cdot)_{M_\psi} : \mathbb{C}_K^G \times \mathbb{C}_K^G \rightarrow \mathbb{C}$ defined by

$$(\Phi, \Psi)_{M_\psi} = (\mathcal{T}_{M_\psi}[\Phi], \mathcal{T}_{M_\psi}[\Psi])_{\mathbb{L}_2(G)}, \quad (4)$$

is an explicit characterization of the inner product on \mathbb{C}_K^G , which is the unique functional Hilbert space with reproducing kernel $K : G \times G \rightarrow \mathbb{C}$ given by

$$K(g, h) = (\mathcal{U}_g \psi, \mathcal{U}_h \psi)_{\mathbb{L}_2(\mathbb{R}^d)} = (\mathcal{U}_{h^{-1}g} \psi, \psi)_{\mathbb{L}_2(\mathbb{R}^d)}, \quad g, h \in G. \quad (5)$$

The wavelet transformation $\mathcal{W}_\psi : H \rightarrow \mathbb{C}_K^G$ given by 

$$\mathcal{W}_\psi[f](\mathbf{b}, t) = (\mathcal{U}_g \psi, f)_{\mathbb{L}_2(\mathbb{R}^d)}, \quad f \in \mathbb{L}_2(\mathbb{R}^d), \quad g = (\mathbf{b}, t) \in \mathbb{R}^d \rtimes_\varphi T, \quad (6)$$

is a unitary mapping from H to \mathbb{C}_K^G . The space \mathbb{C}_K^G is a closed subspace of the Hilbert space $\mathbb{H}_\psi \otimes \mathbb{L}_2(T; \frac{d\mu_T(t)}{\det(\varphi(t))})$, where $\mathbb{H}_\psi = \{f \in H \mid M_\psi^{-\frac{1}{2}} \mathcal{F}[f] \in \mathbb{L}_2(\mathbb{R}^d)\}$ is equipped with the inner product

$$(f_1, f_2) = (M_\psi^{-\frac{1}{2}} \mathcal{F}[f_1], M_\psi^{-\frac{1}{2}} \mathcal{F}[f_2])_{\mathbb{L}_2(\mathbb{R}^d; (2\pi)^{-d/2} d\mathbf{x})}, \text{ for all } f_1, f_2 \in H.$$

The orthogonal projection \mathbb{P}_ψ of $\mathbb{H}_\psi \otimes \mathbb{L}_2(T; \frac{d\mu_T(t)}{\det(\varphi(t))})$ onto \mathbb{C}_K^G is given by $(\mathbb{P}_\psi[\Phi])(g) = (K(\cdot, g), \Phi)_{M_\psi}$.

PROOF. See Appendix A for proof. □

Remark 2. *Since $\mathcal{W}_\psi : H \rightarrow \mathbb{C}_K^G$ is unitary, the inverse equals the adjoint and thus the image f can be reconstructed from the transformed image $\mathcal{W}_\psi[f]$ by*

$$f = \mathcal{W}_\psi^*[\mathcal{W}_\psi[f]] = \mathcal{F}^{-1} \left[\omega \mapsto \frac{1}{(2\pi)^{d/2}} \int_T \mathcal{F}[\mathcal{W}_\psi[f](\cdot, t)](\omega) \mathcal{F}[\mathcal{R}_t \psi](\omega) \frac{d\mu_T(t)}{|\det(\varphi(t))|} M_\psi^{-1}(\omega) \right].$$

2.2. Coherent State Transform on the $SE(2)$ group

In this case $G = SE(2)$, and non-square integrable left-regular representation $(\mathcal{U}_{g=(\mathbf{b}, \theta)} \psi)(\mathbf{x}) = \psi(\mathbf{R}_\theta^{-1}(\mathbf{x} - \mathbf{b}))$, $\Omega = \mathbb{R}^2$ and $H = \mathbb{L}_2(\mathbb{R}^2)$ leading to [18, Thm 1]. For more details on construction as well operators in the coherent state domain see [39, 40]. For $\psi \in \mathbb{L}_2(\mathbb{R}^2) \cap \mathbb{L}_1(\mathbb{R}^2)$, M_ψ is a continuous function vanishing at infinity. Note that $C_\psi \neq M_\psi$ in this case as $M_\psi = 1$ and therefore unitary operator $\mathcal{W}_\psi : \mathbb{L}_2(\mathbb{R}^2) \rightarrow \mathbb{L}_2(SE(2))$ cannot be obtained. In order to deal with \mathbb{L}_2 -isometries one needs to either rely on distributions $\psi \in \mathbb{H}^{-s}(\mathbb{R}^2)$ with $s > 1$ and appropriate distributional wavelet transforms [43, Appendix B] or one needs to restrict to disc-limited images, which is appropriate for imaging applications.

2.3. Continuous Wavelet Transform on $SIM(2)$ group

Consider the case $T := SO(2) \times \mathbb{R}^+$, $G := SIM(2) = \mathbb{R}^2 \rtimes_{\varphi} (SO(2) \times \mathbb{R}^+)$ equipped with the group product

$$(\mathbf{x}, a, \theta)(\mathbf{x}', a', \theta') = (\mathbf{x} + a\mathbf{R}_{\theta}\mathbf{x}', aa', \theta + \theta'), \quad \text{for all } (\mathbf{x}, a, \theta), (\mathbf{x}', a', \theta') \in SIM(2). \quad (7)$$

Consider the unitary representation of $SIM(2)$ in $\mathbb{L}_2(\mathbb{R}^2)$ given by,

$$\mathcal{U}_{g=(\mathbf{b}, a, \theta)}\psi(\mathbf{x}) = \frac{1}{a}\psi\left(\frac{\mathbf{R}_{\theta}^{-1}(\mathbf{x} - \mathbf{b})}{a}\right), \quad a > 0, \theta \in [0, 2\pi], \mathbf{b} \in \mathbb{R}^2, \quad (8)$$

We denote $\mathcal{U} : (\mathbf{x}, t) = (\mathbf{x}, a, \theta) \mapsto \mathcal{U}_{(\mathbf{x}, t)}$ as

$$\mathcal{U}_{(\mathbf{x}, t)}f = \mathcal{T}_{\mathbf{x}}\mathcal{R}_t f, \quad t = (a, \theta) \in \mathbb{R}^+ \times SO(2) \quad (9)$$

where $(\mathcal{T}_{\mathbf{x}}f)(\mathbf{x}') = f(\mathbf{x}' - \mathbf{x})$ and $(\mathcal{R}_t f)(\mathbf{x}') = \frac{1}{a}f(\frac{1}{a}\mathbf{R}_{\theta}\mathbf{x}')$ for all $\mathbf{x}, \mathbf{x}' \in \mathbb{R}^2$. In the continuous setting of $SIM(2)$ Theorem 1 yields

$$M_{\psi}(\boldsymbol{\omega}) = 2\pi \int_0^{2\pi} \int_{\mathbb{R}} |\hat{\psi}(e^{\tau}\mathbf{R}_{\theta}^{-1}\boldsymbol{\omega})|^2 d\tau d\theta = C_{\psi}, \quad \text{with } \hat{\psi} = \mathcal{F}\psi \quad (10)$$

and the reconstruction formula coincides with the known results on unitary CW transforms [35, 23].

2.4. Discrete Implementation

In this subsection we deal with the practical aspects of the implementation of the continuous wavelet transform discussed earlier. Recall that $SIM(2) = \mathbb{R}^2 \rtimes (SO(2) \times \mathbb{R}^+)$. We can replace $SO(2)$ to be a finite rotation group, denoted by \mathbb{T}_N (equipped with the discrete topology) which is locally compact i.e.

$$\mathbb{T}_N = \{e^{iks_{\varphi}} | k \in \{0, 1, \dots, N-1\}, s_{\varphi} = \frac{2\pi}{N}\}, \quad \text{for } N \in \mathbb{N}, \quad (11)$$

and obtain $SE(2, N)$, see [44] for details. On the other hand the scaling group \mathbb{R}^+ cannot be written in terms of a finite scaling group as every finite subgroup of a multiplicative group of a field is a cyclic subgroup. From a practical point of view in the discrete case we need to have a lower and an upper bound on the choice of scales. We assume that $a \in [a^-, a^+]$ where $0 < a^- < a^+$ and consider the following discretization:

$$\mathbb{D}_M = \left\{ e^{(\tau^- + ls_{\rho})} \mid l \in \{0, 1, \dots, M-1\}, s_{\rho} = \frac{\tau^+ - \tau^-}{M} \right\}, \quad \text{for } M \in \mathbb{N}, \quad (12)$$

where $\tau^- = \log(a^-)$ and $\tau^+ = \log(a^+)$. Scale discretization may lead to a sampling problem, see [21, Section 9.2.5] for details in the context of wavelets on the sphere. Using the notation $\theta_k = ks_{\varphi}$ and $a_l = a^- e^{ls_{\rho}}$ we write the discrete version of (9):

$$U_f^{N, M}(\mathbf{b}, a_l, \theta_k) = (\mathcal{T}_{\mathbf{b}}\mathcal{R}_{(a_l, \theta_k)}\psi, f)_{\mathbb{L}_2(\mathbb{R}^2)}, \quad (13)$$

which is the discrete version of wavelet transform of an image $f \in \mathbb{L}_2(\mathbb{R}^2)$. The discrete version of M_{ψ} is,

$$M_{\psi}^D(\boldsymbol{\omega}) = \frac{1}{N} \frac{1}{M} \sum_{k=0}^{N-1} \sum_{l=0}^{M-1} \frac{1}{a_l} |\hat{\psi}((a_l R_{\theta_k})^{-1}\boldsymbol{\omega})|^2. \quad (14)$$

Note that in the discrete setting we are no longer in the unitary irreducible setting of [35] and M_{ψ}^D is not a constant (so $M_{\psi}^D \neq C_{\psi}$). Furthermore the space of wavelet transforms is embedded in $\mathbb{H}_{\psi} \otimes \mathbb{L}_2(SO(2) \times \mathbb{R}^+)$ instead of $\mathbb{L}_2(\mathbb{R}^2 \times SO(2) \times \mathbb{R}^+)$.

2.5. Stable reconstruction of an image from WT

The unitarity result (Theorem 1) with $\mathbb{C}_K^{SIM(2)} \subset \mathbb{H}_\psi \otimes \mathbb{L}_2(SO(2) \times \mathbb{R}^+; \frac{d\mu_T(t)}{\det(\varphi(t))})$ depends on the wavelet ψ . For stability estimates one requires \mathbb{L}_2 -norms on both the domain and the range. This means we must impose uniform lower and upper bounds in (3), which is possible only when we restrict the space of images to functions in $\mathbb{L}_2(\mathbb{R}^2) \cap \mathbb{L}_1(\mathbb{R}^2)$ whose Fourier transform is supported in an annulus. The space of these images is a Paley-Wiener space given by,

$$\mathbb{L}_2^{\varrho^-, \varrho^+}(\mathbb{R}^2) = \{f \in \mathbb{L}_2(\mathbb{R}^2) \mid \text{supp}(\mathcal{F}[f]) \subset B_{0, \varrho^+} \setminus B_{0, \varrho^-}\}, \quad \varrho^+ > \varrho^- > 0, \quad (15)$$

where B_{0, ϱ^\pm} denotes a ball of radius ϱ^\pm around the origin in the Fourier domain. A practical motivation for the assumption of an upper bound (ϱ^+) on the support of the Fourier transform of the images is the Nyquist theorem, which states that *every band-limited function is determined by its values on a discrete grid*.

We wish to construct a wavelet transform

$$\mathcal{W}_\psi^{\varrho^-, \varrho^+} : \mathbb{L}_2^{\varrho^-, \varrho^+}(\mathbb{R}^2) \rightarrow \mathbb{L}_2(\mathbb{R}^2 \times SO(2) \times \mathbb{R}^+) \quad (16)$$

which requires that (recall Eq.(15)),

$$\mathcal{U}_{\mathbf{x}, a, \theta} \psi \in \mathbb{L}_2^{\varrho^-, \varrho^+}(\mathbb{R}^2), \text{ where } a \in [a^-, a^+] \text{ and } \theta \in [0, 2\pi], \text{ with } a^+ > 1 > a^- > 0 \text{ such that } \frac{\varrho^-}{a^-} < \frac{\varrho^+}{a^+}.$$

We make the choice

$$\psi \in \mathbb{L}_1(\mathbb{R}^2) \cap \mathbb{L}_2(\mathbb{R}^2) \text{ with } \text{supp}(\mathcal{F}[\psi]) \subset B_{0, \varrho^+ / a^+} \setminus B_{0, \varrho^- / a^-} \quad (17)$$

and thus we have $\text{supp}(\mathcal{F}[\mathcal{U}_{\mathbf{x}, a, \theta} \psi]) \subset B_{0, \varrho^+} \setminus B_{0, \varrho^-}$, where $a \in [a^-, a^+]$ and $\theta \in [0, 2\pi]$.

Here $\psi \in \mathbb{L}_2^{\varrho^-, \varrho^+}(\mathbb{R}^2)$ is called an *admissible wavelet* if

$$0 < \widetilde{M}_\psi = (2\pi) \int_0^{2\pi} \int_{a^-}^{a^+} \left| \frac{\mathcal{F}[\mathcal{R}_{a, \theta} \psi]}{\sqrt{\det \varphi(t)}} \right|^2 \frac{da}{a} d\theta < \infty \text{ on } B_{0, \varrho^+} \setminus B_{0, \varrho^-}, \quad (18)$$

where $\varphi(t)\mathbf{x} = \varphi(a, \theta)\mathbf{x} = a\mathbf{R}_\theta\mathbf{x}$, and note that $M_\psi = C_\psi \neq \widetilde{M}_\psi$. By compactness of $[-\pi, \pi] \times [a^-, a^+]$, Eq.(17) and Fubini's theorem, M_ψ is a continuous function vanishing at ∞ . We define, $SIM_+^- := \mathbb{R}^2 \times [-\pi, \pi] \times [a^-, a^+]$.

Definition 3. *Let ψ be an admissible wavelet in the sense of (18). Then the wavelet transform $\mathcal{W}_\psi^{\varrho^-, \varrho^+} : \mathbb{L}_2^{\varrho^-, \varrho^+}(\mathbb{R}^2) \rightarrow \mathbb{L}_2(SIM_+^-)$ is given by*

$$(\mathcal{W}_\psi^{\varrho^-, \varrho^+}[f])(g) = \frac{1}{a} \int_{\mathbb{R}^2} \overline{\psi\left(R_\theta^{-1}\left(\frac{\mathbf{y} - \mathbf{x}}{a}\right)\right)} f(\mathbf{y}) d\mathbf{y}, \quad f \in \mathbb{L}_2^{\varrho^-, \varrho^+}(\mathbb{R}^2),$$

for almost every $g = (\mathbf{x}, a, \theta) \in SIM_+^-$.

Quantification of Stability We quantify stability of an invertible linear transformation $A : V \rightarrow W$ from a Banach space $(V, \|\cdot\|_V)$ to a Banach space $(W, \|\cdot\|_W)$ via the condition number

$$\text{cond}(A) = \|A^{-1}\| \|A\| = \left(\sup_{\mathbf{x} \in V} \frac{\|\mathbf{x}\|_V}{\|A\mathbf{x}\|_W} \right) \left(\sup_{\mathbf{x} \in V} \frac{\|A\mathbf{x}\|_W}{\|\mathbf{x}\|_V} \right) \geq 1. \quad (19)$$

The closer it approximates 1, the more stable the operator and its inverse is. The condition number depends on the norms imposed on V and W . From a practical point of view, it is appropriate to impose the $\mathbb{L}_2(SIM_+^-)$ -norm instead of the reproducing kernel norm since it does not depend on the choice of the wavelet ψ and we also use a \mathbb{L}_2 -norm on the space of images.

Theorem 4. Let ψ be an admissible wavelet in the sense of (18), with $\widetilde{M}_\psi(\boldsymbol{\omega}) > 0$ for all $\boldsymbol{\omega} \in B_{0,\varrho^+} \setminus B_{0,\varrho^-}$. Then the condition number $\text{cond}(\mathcal{W}_\psi^{\varrho^-, \varrho^+})$ of $\mathcal{W}_\psi^{\varrho^-, \varrho^+} : \mathbb{L}_2^{\varrho^-, \varrho^+}(\mathbb{R}^2) \rightarrow \mathbb{L}_2(G)$, ($G = \text{SIM}_+^-$) defined by

$$\text{cond}(\mathcal{W}_\psi^{\varrho^-, \varrho^+}) = \|(\mathcal{W}_\psi^{\varrho^-, \varrho^+})^{-1}\| \|(\mathcal{W}_\psi^{\varrho^-, \varrho^+})\| = \left(\sup_{f \in \mathbb{L}_2^{\varrho^-, \varrho^+}(\mathbb{R}^2)} \frac{\|f\|_{\mathbb{L}_2(\mathbb{R}^2)}}{\|U_f\|_{\mathbb{L}_2(G)}} \right) \left(\sup_{f \in \mathbb{L}_2^{\varrho^-, \varrho^+}(\mathbb{R}^2)} \frac{\|U_f\|_{\mathbb{L}_2(G)}}{\|f\|_{\mathbb{L}_2(\mathbb{R}^2)}} \right)$$

satisfies

$$1 \leq (\text{cond}(\mathcal{W}_\psi^{\varrho^-, \varrho^+}))^2 \leq \left(\max_{\varrho^- \leq \|\boldsymbol{\omega}\| \leq \varrho^+} \widetilde{M}_\psi^{-1}(\boldsymbol{\omega}) \right) \left(\max_{\varrho^- \leq \|\boldsymbol{\omega}\| \leq \varrho^+} \widetilde{M}_\psi(\boldsymbol{\omega}) \right).$$

PROOF. The proof is similar to [13, Theorem 20]. For details see [32].

Corollary 5. The stability of the (inverse) wavelet transformation $\mathcal{W}_\psi^{\varrho^-, \varrho^+} : \mathbb{L}_2^{\varrho^-, \varrho^+}(\mathbb{R}^2) \rightarrow \mathbb{L}_2(\text{SIM}_+^-)$ is optimal if $\widetilde{M}_\psi(\boldsymbol{\omega}) = \text{constant}$ for all $\boldsymbol{\omega} \in \mathbb{R}$, with $\varrho^- \leq \|\boldsymbol{\omega}\| \leq \varrho^+$.

In case $\widetilde{M}_\psi \approx 1_{B_{0,\varrho^+} \setminus B_{0,\varrho^-}}$, the reconstruction formula can be simplified to,

$$f \approx \mathcal{F}^{-1} \left[\boldsymbol{\omega} \mapsto \frac{1}{(2\pi)} \int_{a^-}^{a^+} \int_0^{2\pi} \mathcal{F}[U_f(\cdot, a, e^{i\theta})](\boldsymbol{\omega}) \mathcal{F}[\mathcal{R}_{a, e^{i\theta}} \psi](\boldsymbol{\omega}) d\theta \frac{da}{a} \right]. \quad (20)$$

2.6. Design of Proper Wavelets

In the sequel a wavelet $\psi \in \mathbb{L}_2(\mathbb{R}^2) \cap \mathbb{L}_1(\mathbb{R}^2)$ with \widetilde{M}_ψ smoothly approximating $1_{B_{0,\varrho^+} \setminus B_{0,\varrho^-}}$, is called a **proper wavelet**. The entire class of proper wavelets allows for freedom in the choice of ψ . In practice it is mostly sufficient to consider wavelets that are similar to the long elongated patch one would like to detect and orthogonal to structures of local patches which should not be detected. We restrict the possible choices by listing below certain practical requirements to be fulfilled by our transform.

1. The wavelet transform should yield a finite number of orientations (N) and scales (M).
2. The wavelet should be strongly directional, in order to obtain sharp responses on oriented structures.
3. The transformation should handle lines, contours and oriented patterns. Thus the wavelet should pick up edge, ridge and periodic profiles.
4. In order to pick up local structures, the wavelet should be localized in spatial domain.

To ensure that the wavelet is strongly directional and minimizes uncertainty in $\text{SIM}(2)$, we require that the support of the wavelet be contained in a convex cone in the Fourier domain, [19]. The following lemma gives a simple but practical approach to obtain proper wavelets ψ , with $M_\psi = 1_{B_{0,\varrho^+} \setminus B_{0,\varrho^-}}$.

Lemma 6. Let τ^-, τ^+ be chosen such that $\tau^- = \log(a^-)$ and $\tau^+ = \log(a^+)$, where $0 < a \in [a^-, a^+]$ is the finite interval of scaling. Let $A : [0, 2\pi) \rightarrow \mathbb{R}^+$ and $B : [\varrho^-, \varrho^+] \rightarrow \mathbb{R}^+$ such that

$$2\pi \int_0^{2\pi} A(\varphi) d\varphi = 1, \quad \int_{\varrho^-}^{\varrho^+} B(\rho) \rho^{-1} d\rho = 1, \quad (21)$$

then the wavelet $\psi = \mathcal{F}^{-1}[\boldsymbol{\omega} \rightarrow \sqrt{A(\varphi)B(\rho)}]$ has $\widetilde{M}_\psi(\boldsymbol{\omega}) = 1$ for all $\boldsymbol{\omega} = (\rho \cos \varphi, \rho \sin \varphi) \in B_{0,\varrho^+} \setminus B_{0,\varrho^-}$.

PROOF. From (10) and (18), for all $\boldsymbol{\omega} \in B_{0,\varrho^+} \setminus B_{0,\varrho^-}$ we have, with $\tau = \log a$, $\varrho^+ / a^- \leq \rho \leq \varrho^+ / a^+$ by Eq. (17).

$$M_\psi(\boldsymbol{\omega}) = 2\pi \int_0^{2\pi} \int_{\tau^-}^{\tau^+} |\hat{\psi}(e^\tau \mathbf{R}_\theta^{-1} \boldsymbol{\omega})|^2 d\tau d\theta = 2\pi \int_0^{2\pi} \int_{\tau^-}^{\tau^+} |\sqrt{A(\varphi - \theta)B(e^\tau \rho)}|^2 d\tau d\theta = 1. \quad \square$$

Lemma 6 can be translated into the discrete framework, recall (11) and (12), making condition (21),

$$\frac{1}{N} \sum_{k=0}^{N-1} A(\varphi - \theta_k) = 1 \text{ and } \frac{1}{M} \sum_{l=0}^{M-1} B(e^{\tau_l} \rho) = 1. \quad (22)$$

where we have made use of discrete notations introduced in (13). If $2\pi \int_0^{2\pi} \sqrt{A(\varphi)} d\varphi \approx 1$ and $\int_{\tau^-}^{\tau^+} \sqrt{B(\rho)} \rho^{-1} d\rho \approx 1$, we have a fast and simple approximative reconstruction:

$$\begin{aligned} \tilde{f}(\mathbf{x}) &= 2\pi \int_{\tau^-}^{\tau^+} \int_0^{2\pi} (\mathcal{W}_\psi f)(\mathbf{x}, \tau, \theta) d\theta d\tau \approx \mathcal{F}^{-1}[\boldsymbol{\omega} \mapsto (\sqrt{\widetilde{M}_\psi} * \mathcal{F}[f])(\boldsymbol{\omega})](\mathbf{x}), \text{ for a.e. } \boldsymbol{\omega} \in B_{0, \varrho^+} \setminus B_{0, \varrho^-}. \\ \sqrt{\widetilde{M}_\psi} &\approx 1_{B_{0, \varrho^+} \setminus B_{0, \varrho^-}} \Rightarrow \tilde{f} \approx f \in \mathbb{L}_2^{\varrho^-, \varrho^+}(\mathbb{R}^2). \end{aligned} \quad (23)$$

We need to fulfil the requirement $\widetilde{M}_\psi(\boldsymbol{\omega}) \approx 1$ with an appropriate choice of kernel satisfying the additional condition $\sqrt{\widetilde{M}_\psi} \approx 1$. The idea is to “fill the cake by pieces of cake” in the Fourier domain. In order to avoid high frequencies in the spatial domain, these pieces must be smooth and they must overlap. A choice of B-spline based functions in the angular and the log-radial direction is an appropriate choice for such a wavelet kernel. This design of wavelets in the Fourier domain is similar to the framework of curvelets [25, 26, 27]. However, our decomposition of unity in the Fourier domain is more suited for the subsequent design of left-invariant diffusions in the wavelet domain. The reason for us to choose log-polar B-spline decomposition is that the canonical coordinates of the second kind in $SIM(2)$ are given by

$$\xi = a(x \cos \theta + y \sin \theta), \quad \eta = a(-x \sin \theta + y \cos \theta), \quad \theta, \quad \tau = \log_e a,$$

and it will turn out that our subsequent evolutions, that we will pursue in Section 4, are best expressed in these coordinates. A similar construction which involves mixing different levels of scale selectivity was presented in [45].

The k^{th} order B-spline denoted by B^k is defined as

$$B^k(x) = (B^{k-1} * B^0)(x), \quad B^0(x) = \begin{cases} 1 & \text{if } -1/2 < x < +1/2 \\ 0 & \text{otherwise} \end{cases} \quad (24)$$

with the property that B-splines add up to 1. We propose the following kernel

$$\psi(\mathbf{x}) = \mathcal{F}_{\mathbb{R}^2}^{-1}[\boldsymbol{\omega} \rightarrow \sqrt{A(\varphi)B(\rho)}](\mathbf{x})G_{\sigma_s}(\mathbf{x}), \quad (25)$$

where G_{σ_s} is a Gaussian window that enforces spatial locality cf. requirement 4. $A : \mathbb{T} \rightarrow \mathbb{R}^+$ and $B : [\varrho^-, \varrho^+] \rightarrow \mathbb{R}^+$ are defined as,

$$A(\varphi) = B^k\left(\frac{(\varphi \bmod 2\pi) - \pi/2}{s_\varphi}\right), \quad B(\varrho) = B^k\left(\frac{\log[\varrho]}{s_\rho}\right), \quad (26)$$

where $s_\varphi = \frac{2\pi}{N}$ and $s_\rho = (\log[a^+] - \log[a^-])/M$ where M is the number of chosen scales and a^-, a^+ are predefined scales, based on ϱ^-, ϱ^+ respectively. Note that these log B-splines satisfy

$$\sum_{l=0}^{M-1} B^k\left(\frac{\log[\rho]}{s_\rho} + l + \frac{\tau^-}{s_\rho}\right) = 1 \text{ and } \sum_{l=0}^{M-1} \sqrt{B^k\left(\frac{\log[\rho]}{s_\rho} + l + \frac{\tau^-}{s_\rho}\right)} \approx 1. \quad (27)$$

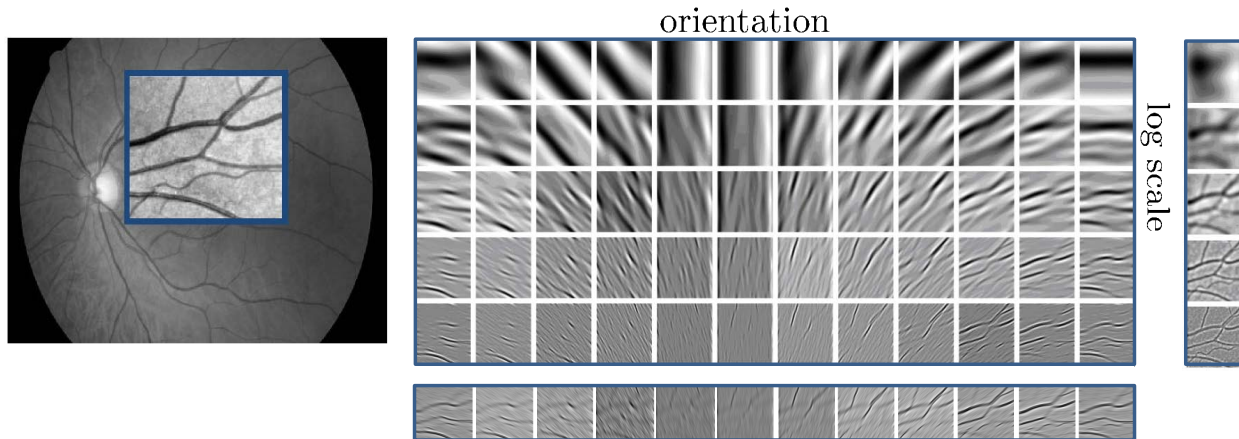


Figure 3: WT of a retinal image. As shown, WT of an image combines the $SE(2)$ -CS transform and Gaussian-Scale Space of the image.

3. Operators on Wavelet Transforms

There exists a 1-to-1 correspondence between bounded operators $\Phi \in \mathcal{B}(\mathbb{C}_K^G)$ on the range of the CW transform and bounded operators $\Upsilon \in \mathcal{B}(\mathbb{L}_2(\mathbb{R}^d))$ given by

$$\Upsilon[f] = (\mathcal{W}_\psi^* \circ \Phi \circ \mathcal{W}_\psi)[f], \quad f \in \mathbb{L}_2(\mathbb{R}^d), \quad (28)$$

which allows us to relate operations on transformed images to operations on images in a robust manner. To get a schematic view of the operations see Figure 1. By Theorem 1 the range of the unitary wavelet transform $\mathcal{W}_\psi : \mathbb{L}_2(\mathbb{R}^2) \rightarrow \mathbb{C}_K^G$ is a subspace of $\mathbb{L}_2(G)$. For proper wavelets we have (approximative) \mathbb{L}_2 -norm preservation and therefore $\mathbb{L}_2(G) \cong \mathbb{H}_\psi$ (with $\mathbb{L}_2(G) = \mathbb{H}_\psi$ if $M_\psi = 1$). In general if, $\Phi : \mathbb{L}_2(G) \rightarrow \mathbb{C}_K^G$ is a bounded operator then the range need not be contained in \mathbb{C}_K^G . Therefore we also consider $\widetilde{\mathcal{W}}_\psi : \mathbb{L}_2(\mathbb{R}^d) \rightarrow \mathbb{L}_2(G)$ given by $\widetilde{\mathcal{W}}_\psi f = \mathcal{W}_\psi f$. Its adjoint is given by,

$$(\widetilde{\mathcal{W}}_\psi)^*(V) = \int_G \mathcal{U}_g \psi V(g) d\mu_G(g), \quad V \in \mathbb{L}_2(G).$$

The operator $\mathbb{P}_\psi = \widetilde{\mathcal{W}}_\psi (\widetilde{\mathcal{W}}_\psi)^*$ is the orthogonal projection on the space \mathbb{C}_K^G whereas $\mathcal{W}_\psi \mathcal{W}_\psi^* = I$. This projection can be used to decompose operator Φ :

$$\Phi(U_f) = \mathbb{P}_\psi(\Phi(U_f)) + (I - \mathbb{P}_\psi)(\Phi(U_f)).$$

Notice that the orthogonal complement $(\mathbb{C}_K^G)^\perp$, which equals range $\mathcal{R}(I - \mathbb{P}_\psi)$, is exactly the null-space of $(\widetilde{\mathcal{W}}_\psi)^*$ as $\mathcal{N}((\widetilde{\mathcal{W}}_\psi)^*) = \mathcal{N}((\mathcal{W}_\psi)^*) = (\mathcal{R}(\mathcal{W}_\psi))^\perp = (\mathbb{C}_K^G)^\perp$ and so

$$[(\widetilde{\mathcal{W}}_\psi)^* \circ \Phi \circ \widetilde{\mathcal{W}}_\psi][f] = [(\widetilde{\mathcal{W}}_\psi)^* \circ \mathbb{P}_\psi \circ \Phi \circ \widetilde{\mathcal{W}}_\psi][f], \quad (29)$$

for all $f \in \mathbb{L}_2(\mathbb{R}^2)$ and all $\Phi \in \mathcal{B}(\mathbb{L}_2(G))$, so we see that the net operator associated to $\Phi : \mathbb{L}_2(G) \rightarrow \mathbb{L}_2(G)$ is given by $\mathbb{P}_\psi \circ \Phi : \mathbb{L}_2(G) \rightarrow \mathbb{C}_K^G$. In the remainder of this section we present design principles for Υ .

3.1. Design Principles

We now formulate a few desirable properties of Υ , and sufficient conditions for Φ that guarantee that Υ meets these requirements.

1. **Covariance with respect to rotation, translation and scaling:**

$$\Upsilon \circ \mathcal{U}_g^{SIM(2)} = \mathcal{U}_g^{SIM(2)} \circ \Upsilon, \quad \forall g = (x, y, \tau, \theta) \in SIM(2). \quad (30)$$

This important because the net operations on images should not be affected by rotation and translation of the original image. This is achieved by restricting one self to left-invariant operators Φ . Often we will omit scaling covariance in Eq.(30) as in many imaging applications this is not natural and therefore we require (30) only to hold for the $SE(2)$ subgroup.

2. **Left-invariant vector fields:** In order to achieve the Euclidean invariance mentioned above, we need to employ left-invariant vector fields on $SIM(2)$ as a moving frame of reference.
3. **Nonlinearity:** The requirement that Υ commute with \mathcal{U} immediately rules out linear operators Φ . Since \mathcal{U} is irreducible by Schur's lemma [46], any linear intertwining operator is a scalar multiple of the identity operator.
4. **Left-invariant parabolic evolutions on the Similitude group:** We consider the following two types of evolutions which include the wavelet transform as a initial condition.
 - Combine linear diffusions with monotone operations on the co-domain
 - Non linear adaptive diffusion
5. **Probabilistic models for contextual multi-scale feature propagation in the wavelet domain:** Instead of uncorrelated soft-thresholding of wavelet coefficients we aim for PDE flows that amplify the wavelet coefficients which are probabilistically coherent w.r.t. neighbouring coefficients. This coherence w.r.t. neighbouring coefficients is based on underlying stochastic processes (random walks) for multiple-scale contour enhancement.

In Subsections 3.2-3.5 we will elaborate on these design principles.

3.2. *Covariance with respect to Rotations and Translations*

Let $G = \mathbb{R}^d \times T$ denote an arbitrary Lie-group.

Definition 7. An operator $\Phi : \mathbb{L}_2(G) \rightarrow \mathbb{L}_2(G)$ is left-invariant iff

$$\Phi[\mathcal{L}_h V] = \mathcal{L}_h[\Phi V], \quad \text{for all } h \in G, V \in \mathbb{L}_2(G), \quad (31)$$

where the left-regular action \mathcal{L}_g of $g \in G$ onto $\mathbb{L}_2(G)$ is given by $\mathcal{L}_h V(g) = V(h^{-1}g)$.

Theorem 8. Let $\Phi : \mathbb{C}_K^G \rightarrow \mathbb{L}_2(G)$ be a bounded operator. Then the unique corresponding operator Υ on H given by $\Upsilon[f] = (\widetilde{\mathcal{W}}_\psi)^* \circ \Phi \circ \widetilde{\mathcal{W}}_\psi[f]$ is Euclidean (and scaling) covariant, i.e. $\mathcal{U}_g \Upsilon = \Upsilon \mathcal{U}_g$ for all $g \in G$ if and only if $\mathbb{P}_\psi \circ \Phi$ is left-invariant, i.e. $\mathcal{L}_g(\mathbb{P}_\psi \circ \Phi) = (\mathbb{P}_\psi \circ \Phi)\mathcal{L}_g$, for all $g \in G$.

PROOF. See [32, Appendix B] which follows the ideas in [13, Theorem 21]. □

Practical Consequence: Now let us return to our case of interest $G = SIM(2)$, where $H = \mathbb{L}_2(\mathbb{R}^2)$. Euclidean invariance of Υ is of great practical importance, since the result of operators on transformed image should not be different if the original image is rotated or translated. In addition in our construction scaling the image also does not affect the outcome of the operation. The latter constraint may not always be desirable.

3.3. *Left-invariant Vector fields (differential operators) on SIM(2)*

Left-invariant differential operators are crucial in the construction of appropriate left-invariant evolutions on $G = SIM(2)$. Similar to Definition 7, the right regular action \mathcal{R}_g of $g \in G$ onto $\mathbb{L}_2(G)$ is defined by

$$\mathcal{R}_g \phi(h) = \phi(hg), \quad \forall g, h \in G, \phi \in \mathbb{L}_2(G). \quad (32)$$

A vector field considered as a differential operator \mathcal{A} on a group G is called left-invariant if it satisfies

$$\mathcal{A}_g \phi = \mathcal{A}_e(\phi \circ L_g) = \mathcal{A}_e(\phi(g \cdot)),$$

for all smooth functions $\phi \in C_c^\infty(\Omega_g)$, where Ω_g is an open set around $g \in G$, e denotes the unity element and with the left multiplication $L_g : G \rightarrow G$ given by $L_g h = gh$. The linear space of left-invariant vector fields $\mathcal{L}(G)$ equipped with the Lie product $[\mathcal{A}, \mathcal{B}] = \mathcal{A}\mathcal{B} - \mathcal{B}\mathcal{A}$ is isomorphic to $T_e(G)$ by means of the isomorphism,

$$T_e(G) \ni A \leftrightarrow \mathcal{A} \in \mathcal{L}(G) \Leftrightarrow \mathcal{A}_g(\phi) = A(\phi \circ L_g) = A(h \mapsto \phi(gh)) =: (L_g)_* A(\phi)$$

for all smooth $\phi : G \supset \Omega_g \rightarrow \mathbb{R}$. We define an operator $d\mathcal{R} : T_e(G) \rightarrow \mathcal{L}(G)$,

$$(d\mathcal{R}(A)\phi)(g) := \lim_{t \downarrow 0} \frac{(\mathcal{R}_{\exp(tA)}\phi)(g) - \phi(g)}{t}, \quad A \in T_e(G), \quad \phi \in \mathbb{L}_2(G), \quad g \in G, \quad (33)$$

and where \mathcal{R} and \exp are the right regular representation and the exponential map respectively. The explicit left-invariant vector fields on $SIM(2)$ are

$$\{\mathcal{A}_1, \mathcal{A}_2, \mathcal{A}_3, \mathcal{A}_4\} = \{\partial_\theta, \partial_\xi, \partial_\eta, a\partial_a\} = \{\partial_\theta, e^\tau(\cos\theta\partial_x + \sin\theta\partial_y), e^\tau(-\sin\theta\partial_x + \cos\theta\partial_y), \partial_\tau\}, \quad (34)$$

where we use the short notation $\partial_x := \frac{\partial}{\partial x}$ for the partial derivatives and with $a = e^\tau$ as introduced in Section 2.4. The set of differential operators $\{\mathcal{A}_1, \mathcal{A}_2, \mathcal{A}_3, \mathcal{A}_4\} = \{\partial_\theta, \partial_\xi, \partial_\eta, \partial_\tau\}$ is the appropriate set of differential operators to be used on CW transformed images since all $SIM(2)$ -coordinate independent linear and nonlinear combinations of these operators are left-invariant. Furthermore at each scale ∂_ξ is always the spatial derivative tangent to the orientation θ and ∂_η is always orthogonal to this orientation. So the left-invariant vector fields provide the appropriate moving frame of reference in the WT domain. See [47, Figure 2.6] for an intuitive illustration. The left-invariant differential operators do not commute:

$$[A_i, A_j] = \sum_{k=1}^4 c_{ij}^k A_k \leftrightarrow [\mathcal{A}_i, \mathcal{A}_j] = \mathcal{A}_i \mathcal{A}_j - \mathcal{A}_j \mathcal{A}_i = \sum_{k=1}^4 c_{ij}^k \mathcal{A}_k, \quad (35)$$

with $A_i = \mathcal{A}_i|_e$, $\mathcal{A}_i = d\mathcal{R}(A_i)$ and c_{ij}^k are the structure constants. An exponential curve is obtained by using the **exp** mapping of the Lie algebra elements

$$\gamma_c(t) = \exp\left(t \sum_{i=1}^4 c^i \mathcal{A}_i \Big|_{g=e}\right) = \exp\left(t \sum_{i=1}^4 c^i A_i\right), \quad (36)$$

and an exponential curve passing through $g_0 \in SIM(2)$ can be obtained by left multiplication with $g_0 = (x_0, y_0, e^{\tau_0}, \theta_0)$, i.e. $g_0 \gamma_c(t)$. The following theorem applies the method of characteristics (for PDEs) to transport along exponential curves. The explicit formulation is important because left-invariant convection-diffusion on $SIM(2)$ takes place only along exponential curves, see [32, Theorem 22].

Theorem 9. *Let $A \in T_e(SIM(2))$. Then the following holds.*

- (1) $U \in \mathcal{D}(d\mathcal{R}(A)) \Rightarrow \mathcal{R}_{e^{tA}} U \in \mathcal{D}(d\mathcal{R}(A))$, where $\mathcal{D}(X)$ denotes the domain of operator X .
- (2) $e^{td\mathcal{R}(A)} = \mathcal{R}_{e^{tA}}, \forall t > 0$ where $d\mathcal{R}$ is defined in (33).
- (3) $\gamma_c(t) = g_0 \exp\left(t \sum_{i=1}^4 c^i A_i\right)$ are the characteristics for the following PDE,

$$\frac{\partial W(g, t)}{\partial t} = - \sum_{i=1}^4 c^i \mathcal{A}_i W(g, t), \quad W(g, 0) = U. \quad (37)$$

PROOF. See [32, Appendix D] for proof.

The exponential map defined on $T_e(SIM(2))$ is bijective, and so we can define the logarithm mapping, $\log = (\exp)^{-1} : SIM(2) \rightarrow T_e(SIM(2))$. For proof see [21, Chap. 4]. For the explicit formulation of the exponential and logarithm curves in our case see Appendix B. The explicit form of the log map will be used to approximate the solution for linear evolutions on $SIM(2)$ in Section 4.1.

3.4. Quadratic forms on left-invariant vector fields

We apply the general theory of evolutions (convection-diffusion) on Lie groups, [10], to the $SIM(2)$ group and consider the following left-invariant second-order evolution equations,

$$\begin{cases} \partial_t W(g, t) = Q^{\mathbf{D}, \mathbf{a}}(\mathcal{A}_1, \mathcal{A}_2, \mathcal{A}_3, \mathcal{A}_4)W(g, t), & g \in SIM(2), t > 0 \\ W(\cdot, t = 0) = \mathcal{W}_\psi f(\cdot), \end{cases} \quad (38)$$

where $W : SIM(2) \times \mathbb{R}^+ \rightarrow \mathbb{C}$ and $Q^{\mathbf{D}, \mathbf{a}}$ is given by

$$Q^{\mathbf{D}, \mathbf{a}}(\mathcal{A}_1, \mathcal{A}_2, \mathcal{A}_3, \mathcal{A}_4) = \sum_{i=1}^4 \left(-a_i \mathcal{A}_i + \sum_{j=1}^4 D_{ij} \mathcal{A}_i \mathcal{A}_j \right), \quad a_i, D_{ij} \in \mathbb{R}, \mathbf{D} := [D_{ij}] \geq 0, \mathbf{D}^T = \mathbf{D}. \quad (39)$$

For now consider the case where \mathbf{D} is diagonal and $a_1 = a_2 = a_4 = 0$. This is a natural choice when a_i and D_{ij} are constant, as we do not want to impose a-priori curvature and a-priori scaling drifts in our flows. However, when adapting \mathbf{D} and \mathbf{a} to the initial condition (i.e. wavelet transform data) such restrictions are not necessary. In fact, practical advantages can be obtained when choosing \mathbf{D} diagonal w.r.t. an optimal gauge frame, [7, 40]. Choosing $D_{ij} = D_{ii} \delta_{ij}$, $i, j \in \{1, 2, 3, 4\}$, the quadratic form becomes,

$$Q^{\mathbf{D}, \mathbf{a}}(\mathcal{A}_1, \mathcal{A}_2, \mathcal{A}_3, \mathcal{A}_4) = [-a_1 \partial_\theta - a_2 \partial_\xi - a_3 \partial_\eta - a_4 \partial_\tau + D_{11}(\partial_\theta)^2 + D_{22}(\partial_\xi)^2 + D_{33}(\partial_\eta)^2 + D_{44}(\partial_\tau)^2]. \quad (40)$$

The first order part of (40) takes care of transport (convection) along the exponential curves, deduced in Section 3.3. The second order part takes care of diffusion in the $SIM(2)$ group. Application of the Hörmander's theorem [48] to the full convection-diffusion system produces necessary and sufficient conditions for smooth (resolvent) Green's functions on $SIM(2) \setminus \{e\}$ on the diffusion and convection parameters (\mathbf{D}, \mathbf{a}) :

$$\{1, 2, 4\} \subset \{i \mid a_i \neq 0 \vee D_{ii} \neq 0\} \vee \{1, 3, 4\} \subset \{i \mid a_i \neq 0 \vee D_{ii} \neq 0\}. \quad (41)$$

In the remainder of this article we will not include convection (i.e. $\mathbf{a} = \mathbf{0}$).

A covariant derivative of a co-vector field \mathbf{a} on the tangent bundle $T(SIM(2))$ is a $(0, 2)$ -tensor field with components $\nabla_j a_i = \mathcal{A}_j a_i - \Gamma_{ij}^k a_k$, whereas the covariant derivative of a vector field \mathbf{v} on $SIM(2)$ is a $(1, 1)$ -tensor field with components $\nabla_{j'} v^i = \mathcal{A}_{j'} v^i + \Gamma_{j'k}^i v^{k'}$, where $\nabla_j := D_{\mathcal{A}_j}$, when imposing the Cartan connection. The Christoffel symbols equal minus the (anti-symmetric) structure constants of the Lie algebra $\mathcal{L}(SIM(2))$, i.e. $\Gamma_{ij}^k = -c_{ij}^k$. The left-invariant equations (38) with a diagonal diffusion tensor (40) can be rewritten in covariant derivatives as

$$\begin{cases} \partial_s W(g, s) = \sum_{i,j=1}^4 \mathcal{A}_i((D_{ij}(W))(g, s)) \mathcal{A}_j W(g, s) = \sum_{i,j=1}^4 \nabla_i((D_{ij}(W))(g, s)) \nabla_j W(g, s), \\ W(g, 0) = \mathcal{W}_\psi f(g), \text{ for all } g \in SIM(2), s > 0. \end{cases} \quad (42)$$

Both convection and diffusion in the left-invariant evolution equations (38) (even in the nonlinear setting where the diffusion-matrix \mathbf{D} depends on the data W locally) take place along the exponential curves in $SIM(2)$ which are covariantly constant curves, see [32, Appendix F] for details.

3.5. Probabilistic models for contextual feature propagation

Section 3.4 described the general form of convection-diffusion operators on the $SIM(2)$ group. For the particular case of contour enhancement i.e. diffusion on the $SIM(2)$ group, which corresponds to the choice $D_{ij} = D_{ii} \delta_{ij}$, $i, j \in \{1, 2, 3, 4\}$, $D_{33} = 0$ and $\mathbf{a} = \mathbf{0}$, we have the following result.

Theorem 10. *The evolution on $SIM(2)$ given by*

$$\begin{cases} \partial_t W(g, t) = [D_{11}(\partial_\theta)^2 + D_{22}(\partial_\xi)^2 + D_{44}(\partial_\tau)^2]W(g, t), \\ W(\cdot, t = 0) = \mathcal{W}_\psi f(\cdot), \end{cases} \quad (43)$$

is the forward Kolmogorov (Fokker-Planck) equation of the following stochastic process for multi-scale contour enhancement

$$\begin{cases} \mathbf{X}(s) = \mathbf{X}(0) + \sqrt{2D_{22}}\epsilon_2 \int_0^s (\cos(\Theta(t))e_x + \sin(\Theta(t))e_y) e^{\mathfrak{T}(t)} d(\sqrt{t}) \\ \Theta(s) = \Theta(0) + \sqrt{s}\sqrt{2D_{11}}\epsilon_1 \\ \mathfrak{T}(s) = \mathfrak{T}(0) + \sqrt{s}\sqrt{2D_{44}}\epsilon_4, \end{cases} \quad (44)$$

where $\epsilon_1, \epsilon_2, \epsilon_4 \sim \mathcal{N}(0, 1)$ are the standard random variables and $D_{11}, D_{22}, D_{44} > 0$.

In order to avoid technicalities regarding probability measures on Lie groups, see [49] for details, we only provide a short and basic explanation which covers the essential idea of the proof. The stochastic differential equation in (44) can be considered as limiting case of the following discrete stochastic processes on $SIM(2)$:

$$\begin{cases} G_{n+1} := (\mathbf{X}_{n+1}, \Theta_{n+1}, \mathfrak{T}_{n+1}) = G_n + \sqrt{\Delta s} \sum_{i=1,2,4} \sum_{j=1,2,4} \frac{\epsilon_{i,n+1}}{\sqrt{N}} \sqrt{2D_{ii}} e_i|_{G_n}, \\ G_0 = (\mathbf{X}_0, \Theta_0, \mathfrak{T}_0), \end{cases} \quad (45)$$

where $n = 1, \dots, N-1, N \in \mathbb{N}$ denotes the number of steps with step-size $\Delta s > 0$, $\{\epsilon_{i,n+1}\}_{i=1,2,4}$ are independent normally distributed $\epsilon_{i,n+1} \sim \mathcal{N}(0, 1)$ and $e_j|_{G_n} \equiv \mathcal{A}_j|_{G_n}$, i.e.

$$e_1|_{G_n} = \begin{pmatrix} 0 \\ 0 \\ 0 \\ 1 \end{pmatrix}, \quad e_2|_{G_n} = \begin{pmatrix} e^{\mathfrak{T}} \cos \Theta \\ e^{\mathfrak{T}} \sin \Theta \\ 0 \\ 0 \end{pmatrix}, \quad e_3|_{G_n} = \begin{pmatrix} -e^{\mathfrak{T}} \sin \Theta \\ e^{\mathfrak{T}} \cos \Theta \\ 0 \\ 0 \end{pmatrix}, \quad e_4|_{G_n} = \begin{pmatrix} 0 \\ 0 \\ 1 \\ 0 \end{pmatrix}.$$

The continuous process (44) arises from the discrete process (45) by recursion and taking the limit $N \rightarrow \infty$.

4. Left-invariant Diffusions on $SIM(2)$

Following our framework of stochastic left-invariant evolutions on $SIM(2)$ we will restrict ourselves to contour enhancement, where the Forward-Kolmogorov equation is essentially a hypo-elliptic diffusion on the $SIM(2)$ group and therefore we recall Eq.(43). In the remainder of this paper we study linear diffusion (combined with monotone operations on the co-domain) and non-linear diffusion on the $SIM(2)$ group in the context of our imaging application.

4.1. Approximate Contour Enhancement Kernels for Linear Diffusion on WT

In [38, 39], the authors derive the exact Green's function of (38) for the $SE(2)$ case. To our knowledge explicit and exact formulae for heat kernels of linear diffusion on $SIM(2)$ do not exist in the literature. However using the general theory in [50, 51], one can compute Gaussian estimates for Green's function of left-invariant diffusions on Lie groups. Following the idea of contraction explained in [32, Appendix E] and the general theory in [51] one can derive the following smooth estimates for the Greens' function

$$|K_t^{\mathbf{D}}(g)| \leq \frac{1}{4\pi t^{\frac{5}{2}} D_{11} D_{22} \sqrt{D_{44}}} \exp \left(\frac{-1}{4t} \left(\left[\frac{\theta^2}{D_{11}} + \frac{(c^2(g))^2}{D_{22}} + \frac{\tau^2}{D_{44}} \right]^2 + \frac{|c^3(g)|^2}{D_{11} D_{22} D_{44}} \right) \right), \quad (46)$$

with $c^2(g) = \frac{(y\theta - x\tau) + (-\theta\eta + \tau\xi)}{t(1 + e^{2\tau} - 2e^{\tau} \cos\theta)}$, $c^3(g) = \frac{-(x\theta + y\tau) + (\theta\xi + \tau\eta)}{t(1 + e^{2\tau} - 2e^{\tau} \cos\theta)}$.

For details on these estimates and the structure of these kernels see [32, Section 4.1].

Remark 11. When cascading group convolutions and transformations in the co-domain of WT one can generalize the scattering operators by Mallat et al. on \mathbb{R}^n , see [52, 53], to left-invariant scattering operators on Lie groups such as $SIM(2)$ which would provide us with stability under local deformations.

In practice, medical images exhibit complicated structures which require local adaptivity per group location via locally adapted frames. This brings us to non-linear diffusions that we will solve numerically next section.

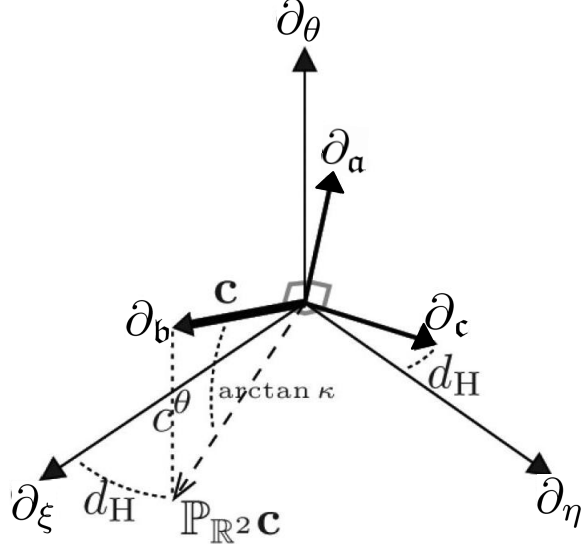


Figure 4: Illustration of curvature κ and deviation from horizontality d_H and the gauge frame. Deviation from horizontality quantifies the local deviation of a curve $t \mapsto \gamma(t) = (\mathbf{x}(t), \theta(t))$ in $SE(2)$ from curve $t \mapsto (\mathbf{x}(t), \arg(\dot{x}(t) + i\dot{y}(t)))$. See (47) on how locally adaptive frame $\{\partial_a, \partial_b, \partial_c\}$ relates to the left-invariant frame $\{\partial_\theta, \partial_\xi, \partial_\eta\}$.

4.2. Nonlinear Left-invariant Diffusions on $SIM(2)$

Adaptive nonlinear diffusion on the 2D Euclidean motion group $SE(2)$, called coherence enhancing diffusion on Coherent state transform¹ (CED-CS) was introduced in [7, 39]. We wish to apply this adaptive $SE(2)$ diffusion to each scale in WT, which is possible because at a fixed scale it is a function on the $SE(2)$ group. Next we present a brief outline of the CED-CS algorithm and then apply it to our case of interest.

4.2.1. CED-CS - Brief Outline

CED-CS involves the following two steps:

- *Curvature Estimation.* Curvature estimation of a spatial curve is based on the optimal exponential curve fit at each point. We find the best exponential curve fit at (x_0, y_0, θ_0) to the absolute value of the data $(x, y, \theta) \mapsto |(\mathcal{W}_\psi f)(x, y, \theta)|$ by using the exponential map via the techniques explained in [40, 7]:

$$t \mapsto (x_0, y_0, \theta_0) \exp(t(c_*^1 A_1 + c_*^2 A_2 + c_*^3 A_3)) \text{ with } (c_*^1)^2 + \beta^2 (c_*^2)^2 + \beta^2 (c_*^3)^2 = 1,$$

where β has physical dimension $[Length]^{-1}$ parameterizing a left-invariant metric on $T(SE(2))$. The absolute value of CS transform is employed for diffusion adaptation as it is phase invariant. As a result best exponential curve fits are uniform along the cross-section of a line.

- *Adaptive curvatures based diffusion scheme using gauge coordinates.* The best exponential curve fit mentioned above is parametrized by $\mathbf{c}_* = (c_*^1, c_*^2, c_*^3) \in \mathbb{R}^3$ which provides us the curvature κ (and deviation from horizontality d_H). In fact it furnishes a whole set of gauge frames $\{\partial_a, \partial_b, \partial_c\}$ as can be seen in Figure 4. The gauge frames in spherical coordinates $(\alpha, d_H) \in [0, \pi] \times [-\pi, \pi]$ are given by

$$\begin{aligned} \partial_a &= -\cos \alpha \cos d_H \partial_\xi - \cos \alpha \sin d_H \partial_\eta + \beta \sin \alpha \partial_\theta, \\ \partial_b &= \sin \alpha \cos d_H \partial_\xi + \sin \alpha \sin d_H \partial_\eta + \beta \cos \alpha \partial_\theta, \quad \partial_c = -\sin d_H \partial_\xi + \cos d_H \partial_\eta. \end{aligned} \tag{47}$$

¹In [7, 39, 40] we have used the acronym CED-OS instead of CED-CS.

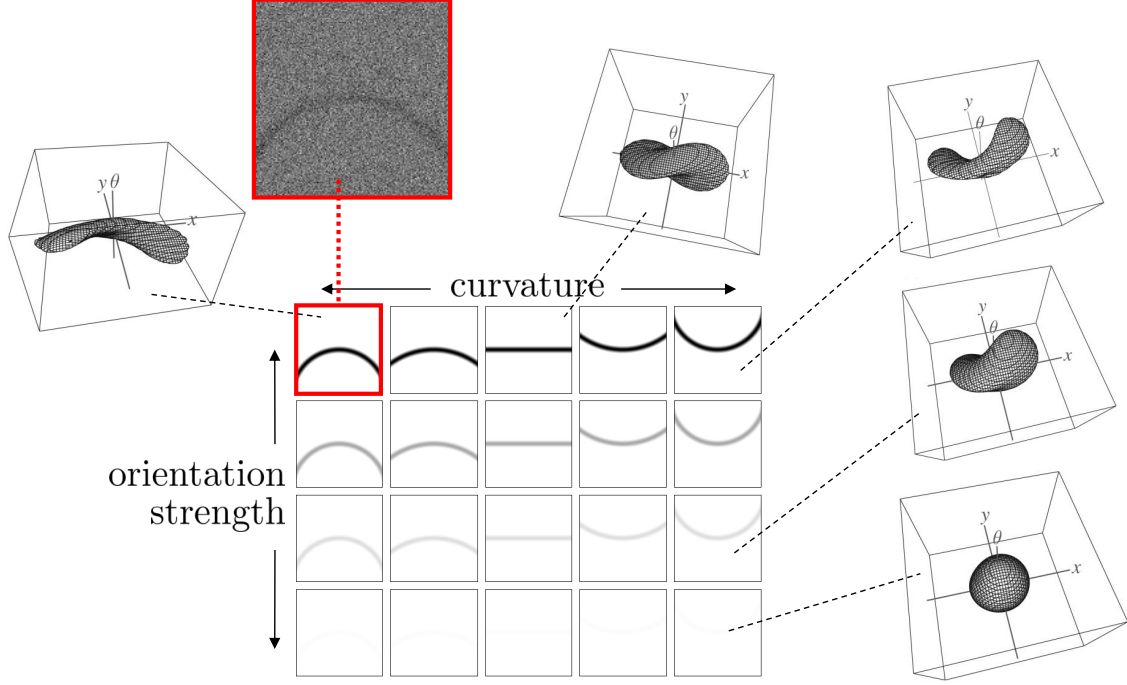


Figure 5: Illustration of heat kernels $K_t^D : SE(2) \rightarrow \mathbb{R}^+$ on $SE(2)$ corresponding to varying curvature and orientation strengths. As orientation strength decreases the kernels become more isotropic (needed for noise reduction) and as curvature increases the diffusion kernels in $SE(2)$ bend accordingly.

The resulting nonlinear evolution equations on the range of $SE(2)$ -CS transform of an image is

$$\begin{cases} \partial_t U(g, t) = \begin{pmatrix} \beta \partial_\theta & \partial_\xi & \partial_\eta \end{pmatrix} M_{\alpha, d_H}^T \begin{pmatrix} D_{aa} & 0 & 0 \\ 0 & D_{bb} & 0 \\ 0 & 0 & D_{cc} \end{pmatrix} M_{\alpha, d_H} \begin{pmatrix} \beta \partial_\theta \\ \partial_\xi \\ \partial_\eta \end{pmatrix} U(g, t), \quad t > 0, \\ U(g, t = 0) = \mathcal{W}_\psi[f](g) \text{ for all } g \in SE(2), \end{cases} \quad (48)$$

where we use the shorthand notation $D_{ii} = (D_{ii}(U))(g, t)$, for $i = \mathbf{a}, \mathbf{b}, \mathbf{c}$. The matrix

$$M_{\alpha, d_H} = \begin{pmatrix} \sin \alpha & -\cos \alpha \cos d_H & -\cos \alpha \sin d_H \\ \cos \alpha & \cos d_H \sin \alpha & \sin \alpha \sin d_H \\ 0 & -\sin d_H & \cos d_H \end{pmatrix}$$

rotates the left-invariant vector fields $\{\beta \partial_\theta, \partial_\xi, \partial_\eta\}$ onto gauge frame $\{\partial_a, \partial_b, \partial_c\}$.

Figure 5 depicts the dependence of the corresponding local linear diffusion kernel on curvature and orientation strengths. Eq.(48) is implemented by a Euler forward scheme (expressed by finite differences along the moving frame of reference while relying on B-spline approximations yielding better rotation covariance [47, Pg.142]) involving the parameters $(\tilde{\rho}, \rho_s, c, \beta)$,

$$U_{n+1} = \Delta t (QU_n) + U_n,$$

where $U_n = U(\cdot, \cdot, t_n)$ with discrete time steps and the generator is given by,

$$(QU)(\cdot, \cdot, t) = \begin{pmatrix} \beta \partial_\theta^D & \partial_\xi^D & \partial_\eta^D \end{pmatrix} M_{\alpha, d_H}^T \left(G_{\rho_s, \rho_s, \rho_s, \beta^2} * \begin{pmatrix} D_{aa}(U(\cdot, \cdot, t)) & 0 & 0 \\ 0 & D_{bb}(U(\cdot, \cdot, t)) & 0 \\ 0 & 0 & D_{cc}(U(\cdot, \cdot, t)) \end{pmatrix} \right) M_{\alpha, d_H} \begin{pmatrix} \beta \partial_\theta^D \\ \partial_\xi^D \\ \partial_\eta^D \end{pmatrix},$$

where $G_{\rho_s, \rho_s, \rho_s \beta^2}(x, y, \theta)$ denotes a Gaussian kernel, which is isotropic on each spatial plane with spatial scale $\rho_s = \frac{1}{2}\sigma_s^2$ and anisotropic with scale $\rho_s \beta^2$ in orientation. Here ∂_j^D denotes the left-invariant finite difference operator in $j = \{\theta, \xi, \eta\}$ direction implemented via B-spline interpolation [7]. Furthermore we set $D_{\mathbf{b}\mathbf{b}} = 1$, $(D_{\mathbf{a}\mathbf{a}}U)(\cdot, \cdot, t) = (D_{\mathbf{c}\mathbf{c}}U)(\cdot, \cdot, t) = e^{-\frac{(s(U)(\cdot, \cdot, t))^2}{c}}$, $c > 0$, with the orientation confidence $s(U(\cdot, \cdot, t)) = (\partial_{\mathbf{a}}^2 + \partial_{\mathbf{c}}^2)U(\cdot, \cdot, t)$, i.e. the Laplacian orthogonal to $\partial_{\mathbf{b}}$ -vector. Within the orientation confidence the derivatives $\partial_{\mathbf{a}}, \partial_{\mathbf{c}}$ are Gaussian derivatives [9], computed with scales $(\tilde{\rho}, \tilde{\rho}, \tilde{\rho}\beta^2)$, orthogonal to locally optimal direction with $\mathbf{c} \equiv \partial_{\mathbf{b}}$ being the eigenvector of the Hessian matrix corresponding to best exponential curve fit, where we enforce horizontality [7] by setting $d_H = 0$ (see Figure 5).

4.2.2. Coherence Enhancing Diffusion on Wavelet Transform (CED-WT)

For an image f in $\mathbb{L}_2(\mathbb{R}^2)$ the corresponding WT is denoted by $\mathcal{W}_\psi(f) \in \mathbb{C}_K^{SIM(2)} \subset \mathbb{L}_2(SIM(2))$ and for any fixed $a \in (0, \infty)$, $\mathcal{W}_\psi(f)(\cdot, \cdot, a, \cdot) \in \mathbb{L}_2(SE(2))$. Let $\Phi_t : \mathbb{L}_2(SE(2)) \rightarrow \mathbb{L}_2(SE(2))$ denote nonlinear adaptive diffusion (CED-CS) on the $SE(2)$ group which is the solution operator of (48) at stopping time t . We propose the operator Φ on the WT defined as

$$(\Phi[(\mathcal{W}_\psi f)])(x, y, a_i, \theta) = \sum_{i=1}^M (\Phi_{t_{a_i}}[\mathcal{W}_\psi f(\cdot, \cdot, a_i, \cdot)])(x, y, \theta), \quad (49)$$

where $(x, y, \theta) \in \mathbb{R}^2 \times [0, 2\pi)$ and $\{a_i\}_{i=1}^M$ is the discretization of $[a^-, a^+]$. Here we make the specific choice of t_{a_i} with $t_{a_i} \leq t_{a_k}$ where $1 \leq i < k \leq M$. The idea here is that on lower scales we have to diffuse more as noise is often dominant at lower scales and therefore lower scales need higher diffusion time.

4.3. Employing the gauge frames for differential invariant features - Vesselness

Retinal vasculature images are highly useful for non-invasive investigation of the quality of the vascular system which is affected in case of diseases such as diabetic retinopathy, glaucoma, hypertension, arteriosclerosis, Alzheimers disease, see [54]. Here accurate and robust detection of the vascular tree is of vital importance [55, 56, 57, 58, 43]. The vascular tree structure in these retinal images is often hard to detect due to low-contrast, noise, the presence of tiny vessels, micro-bleedings and other abnormalities due to diseases, bifurcations, crossings, occurring at multiple scales, and that is precisely where our continuous wavelet framework on $SIM(2)$ and the left-invariant evolutions acting upon them comes into play. In this section we will briefly show some benefits of our framework in terms of multi-scale vesselness filtering, see [59, 60], enhancement and tracking as illustrated in Figures 12 and 13.

Let $f : \mathbb{R}^2 \rightarrow \mathbb{R}$ be a greyscale image. Let $H^s f := G_s * (Hf)$ denote the Hessian of a Gaussian derivative at scale $s = \sigma^2/2$, with eigensystem $E_{\lambda_1} = \langle \mathbf{e}_1 \rangle$, $E_{\lambda_2} = \langle \mathbf{e}_2 \rangle$, with $|\lambda_1| < |\lambda_2|$. Then the vesselness filter is given by

$$\mathcal{V}_{\sigma_1, \sigma_2}^{R, S}(f) = \begin{cases} e^{-\frac{R^2}{2\sigma_1^2}} \left(1 - e^{-\frac{S^2}{2\sigma_2^2}}\right) & \text{if } \lambda_2 > 0, \\ 0 & \text{if } \lambda_2 \leq 0, \end{cases}$$

with anisotropy measure $R = \lambda_1/\lambda_2$ and structureness $S = \lambda_1^2 + \lambda_2^2$. Typically $\sigma_1 = 1/2$ and $\sigma_2 = 0.2\|S\|_\infty$. Now let us rewrite this filter in gauge derivatives $(\partial_\xi^s, \partial_\eta^s)$ where ∂_ξ^s takes the Gaussian derivative along \mathbf{e}_1 at scale $s = \sigma^2/2$ whereas ∂_η^s takes the Gaussian derivative along \mathbf{e}_2 at scale $s = \sigma^2/2$. Then the vesselness filter can be written as

$$\mathcal{V}_{\sigma_1, \sigma_2}(f) = \begin{cases} e^{-\frac{1}{2\sigma_1^2} \left(\frac{f_{\eta\eta}^s}{f_{\xi\xi}^s}\right)^2} \left(1 - e^{-\frac{(f_{\eta\eta}^s)^2 + (f_{\xi\xi}^s)^2}{2\sigma_2^2}}\right) & \text{if } f_{\eta\eta}^s > 0 \\ 0 & \text{if } f_{\eta\eta}^s \leq 0, \end{cases}$$

where subscripts denote partial derivatives and superscripts indicate the scale $s > 0$ over which they are taken. Therefore on the $SE(2)$ -CS transformed image, where we have left-invariant frames $\{\partial_\xi, \partial_\eta, \partial_\theta\}$ with

$\xi = x \cos \theta + y \sin \theta$, $\eta = -x \sin \theta + y \cos \theta$, we propose the vesselness filter on $SE(2)$ -CS transformed image $U := \mathcal{W}_\psi(f)$

$$\mathbf{x} \mapsto \frac{|\mathcal{V}_{\sigma_1, \sigma_2}(U(\cdot, \theta))|(\mathbf{x})}{\max_{(\mathbf{x}, \theta) \in SE(2)} |\mathcal{V}_{\sigma_1, \sigma_2}(U(\cdot, \theta))|(\mathbf{x})} \quad \text{with } \sigma_1 = \frac{1}{2}, \quad \sigma_2 = 0.2 \max_x \Delta_x U(x, \theta) = 0.2 \|S\|_\infty.$$

However, akin to the CED-CS [40] better results are obtained by using a local gauge frame $\{\partial_a, \partial_b, \partial_c\}$ defined in Eq. (47) with the best exponential curve fit. In this case for all $g \in SE(2)$ we have

$$\tilde{\mathcal{V}}_{\sigma_1, \sigma_2}(U) = \begin{cases} e^{-\frac{1}{2\sigma_1^2} \frac{(U_{bb}^s)^2}{(U_{aa}^s + U_{cc}^s)^2}} \left(1 - e^{-\frac{(U_{aa}^s + U_{cc}^s)^2 + (U_{bb}^s)^2}{2\sigma_2^2}} \right) & \text{if } U_{aa}^s + U_{cc}^s > 0 \\ 0 & \text{if } U_{aa}^s + U_{cc}^s \leq 0. \end{cases} \quad (50)$$

We again have anisotropy measure $R = \frac{2\lambda_1}{\lambda_2 + \lambda_3}$, structureness $S = \lambda_1^2 + \frac{(\lambda_2 + \lambda_3)^2}{4}$, $\sigma_1 = \frac{1}{2}$ and $\sigma_2 = 0.2 \|U_{aa}^s + U_{cc}^s\|_\infty$. Then we normalize

$$(V_{\sigma_1, \sigma_2}(U))(g) = \frac{\tilde{\mathcal{V}}_{\sigma_1, \sigma_2}(U)(g)}{\|\tilde{\mathcal{V}}_{\sigma_1, \sigma_2}(U)\|_\infty} \quad (51)$$

to get the result of $SE(2)$ vesselness filter. Finally, when extending the framework to WT of an image $(\mathcal{W}_\psi f)(x, y, \theta, a_l)$ with $a_l = \exp(ls_\rho) a_0$ we apply the $SE(2)$ vesselness filter on each scale layer $(\mathcal{W}_\psi f)(\cdot, \cdot, \cdot, a_l)$ with a_l fixed where we adapt $\sigma_2(a_l) = 0.1 \exp(ls_\rho) \|\mathcal{U}_f(\cdot, \cdot, \cdot, a_l)\|_\infty$.

5. Results

Parameters used for creating WT on images: No. of scales, $M = 4$ (c.f. Eq.12), No. of orientations, $N = 20$. The parameters that we used for CED are (for explanation of parameters see[6]): $\sigma = 0.5$, $\rho = 4$, $C = 1$ and $\alpha = 0.001$. The non-linear diffusion parameters for CED-CS and CED-WT for each scale are: $\rho_s = 12$, $\tilde{\rho} = 1.5$, $\beta = 0.058$ and $c = 0.08$. All the experiments in this section use these parameters (unless otherwise indicated in the caption) and the varying end times are indicated below the images. We have enforced horizontality in the experiments involving CED-CS, see [7] for more details. In this section we compare the proposed algorithm with state of the art denoising algorithms, Non-local Means filter (NLM) [61], Iterative steering kernel regression (ISKR) [62] and Block-matching and 3D filtering (BM3D) [64, 63]. The parameters for these algorithms are optimized for peak signal-to-noise (PSNR) ratio values.

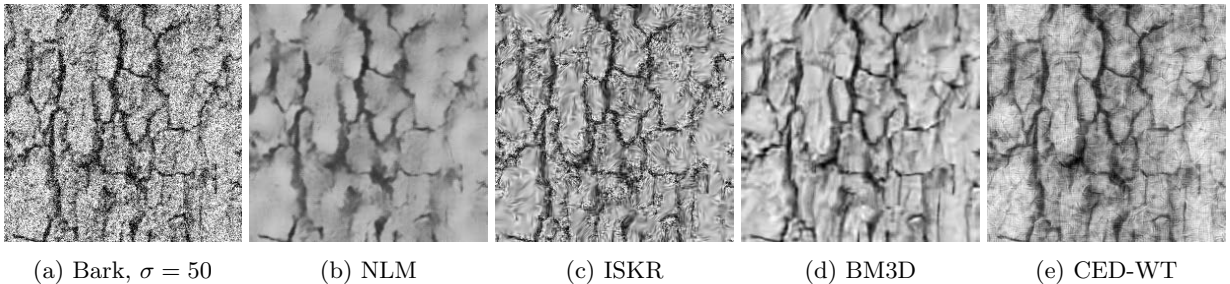


Figure 6: Comparison of CED-WT with state of the art denoising algorithms on a texture image. (a) Brodatz-Bark image with Gaussian noise ($\sigma = 50$). (b) Non-local Means filter [61] (c) Iterative steering kernel regression [62] (d) Block-matching and 3D filtering [63] (e) Coherence enhancing diffusion on Wavelet transform ($t_{a_i} = 0, 0, 4, 5$).



Figure 7: Comparison of CED-WT with state of the art denoising algorithms on Lena image. (a) Lena image with Gaussian noise ($\sigma = 30$) (e) Coherence enhancing diffusion on Wavelet transform ($t_{a_i} = 0, 1, 5, 8$).

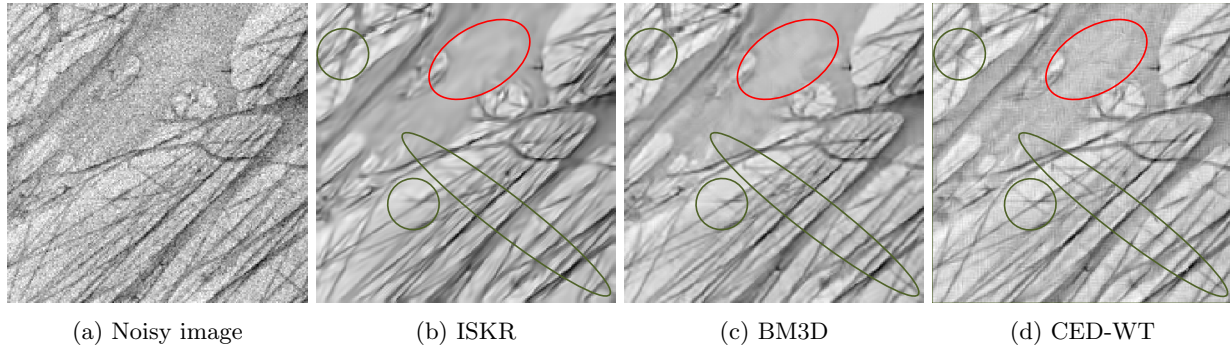


Figure 8: Top: Results of enhancement via on a microscopy image of Collagen fibrin with added Gaussian noise ($\sigma = 20$). Region circled in red indicates that ISKR and BM3D denoise flat regions very well. However ISKR loses crossing structures as indicated by the green circles, where CED-WT retains these structures.

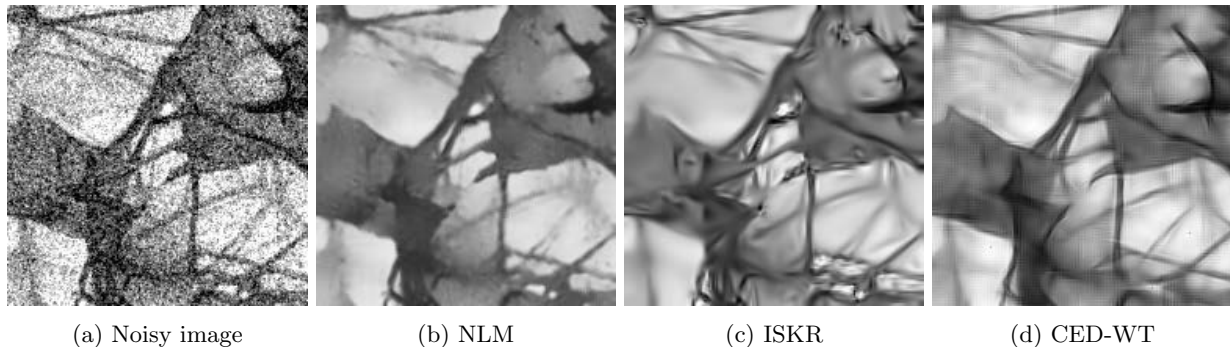


Figure 9: Denoising comparison on an image containing collagen fibres in the Cardiac wall. (a) Noisy input image with correlated noise (b) NLM (c) ISKR (d) CED-WT.

For a comparison of PSNR values see Table 1. Recall Eq.(23) and Eq.(49), which gives the output of CED-WT: $(\Upsilon f)(x, y) = \sum_{i=1}^M \sum_{j=1}^N \frac{2\pi}{N} \frac{(\tau^+ - \tau^-)}{M} \Phi(\mathcal{W}_\psi f)(x, y, a_i, \theta_j)$, where f denotes the noisy input image with $\text{Min}[f] = 0$ and $\text{Max}[f] = 255$. To calculate PSNR values we employ the simple rescaling

$$255 \frac{\Upsilon f - \text{Min}[\Upsilon f]}{\text{Max}[\Upsilon f] - \text{Min}[\Upsilon f]}. \quad (52)$$

In Figure 6 we show enhancements applied to a Brodatz-Bark texture image with Gaussian noise ($\sigma = 50$).

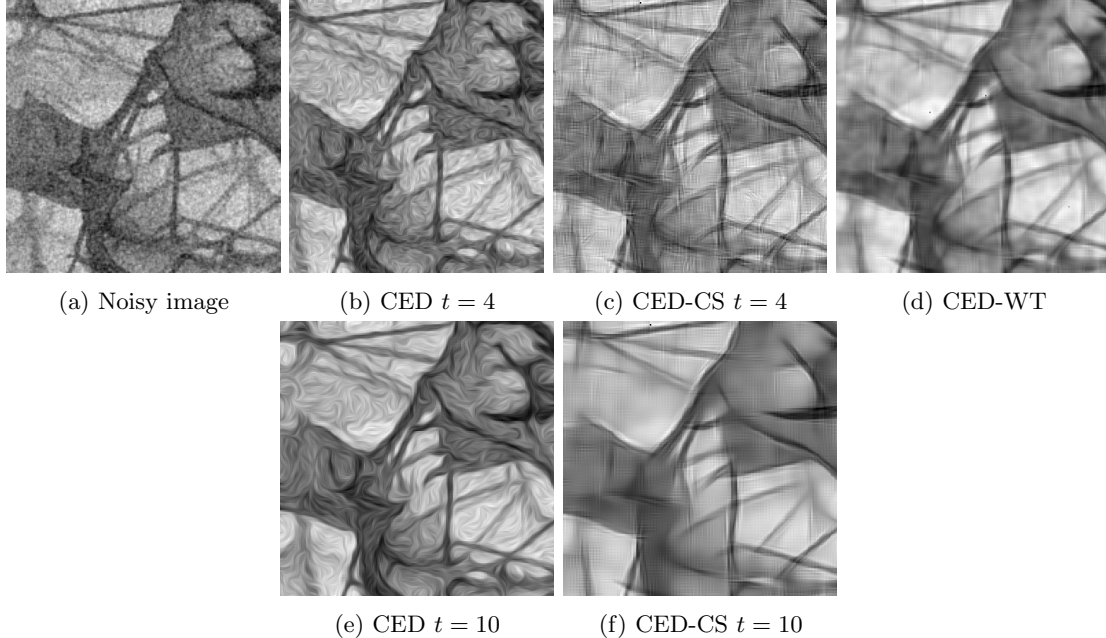


Figure 10: Results of CED, CED-CS and CED-WT on a microscopy image of a Collagen tissue in the cardiac wall. CED-CS exhibits artefacts for small end time, see (c), which vanish if the algorithm is allowed to run longer at the cost of small-scale information, see (f). Therefore best visual results are obtained with CED-WT ($t_{a_i} = 0, 1, 3, 16$).

As CED-WT is a diffusion based method the enhancements involve some blurring. However as our method is based on stochastic line propagation, see Section 3.5, the lines are more coherent as visible in the enhancement.

Figure 7 shows the results of denoising on noisy Lena image ($\sigma = 30$). As indicated by PSNR values in Table 1, though CED-WT does not compete with state of the art at lower noise levels ($\sigma = 30$), it is more robust under higher noise levels and does compete with NLM and ISKR for $\sigma = 50, 60$. At the smaller noise levels further visual improvements of our method could be obtained by including median filtering techniques rather than diffusion techniques at large flat (isotropic) areas.

Figure 8 compares enhancements on a microscopy image of collagen fibrin with added Gaussian noise ($\sigma = 20$). The region circled in red indicates that ISKR and BM3D perform better in denoising on flat regions. The green regions point out loss in multiple-scale crossing structures in ISKR, BM3D compared to CED-WT.

In Figure 9 we consider a typical example of a medical imaging application containing crossing lines at various scales in a medical (2-photon microscopy) image. These kind of images are acquired in tissue engineering research where the goal is to e.g. create artificial heart valves [65]. On these images we obtain clear visual improvements over the state of the art denoising algorithms (NLM and ISKR) as we appropriately deal with multiple scale crossings. Furthermore, to illustrate the potential of the currently proposed algorithm over previous works on crossing preserving diffusion and coherence enhancing diffusion we have included Figure 10.

We also ran our algorithm on an image containing collagen fibers within bone tissue in Figure 11. Here the loss of small-scale data in CED-CS compared to CED-WT is evident, and indeed a basic tracking algorithm (based on [34] involving thresholding $\partial_\eta^2 \mathcal{W}_\psi f$ and a basic morphological component method) reveals the benefit: “Tracking on CED-WT outperforms tracking on CED-CS”, see Figure 11. On the other hand

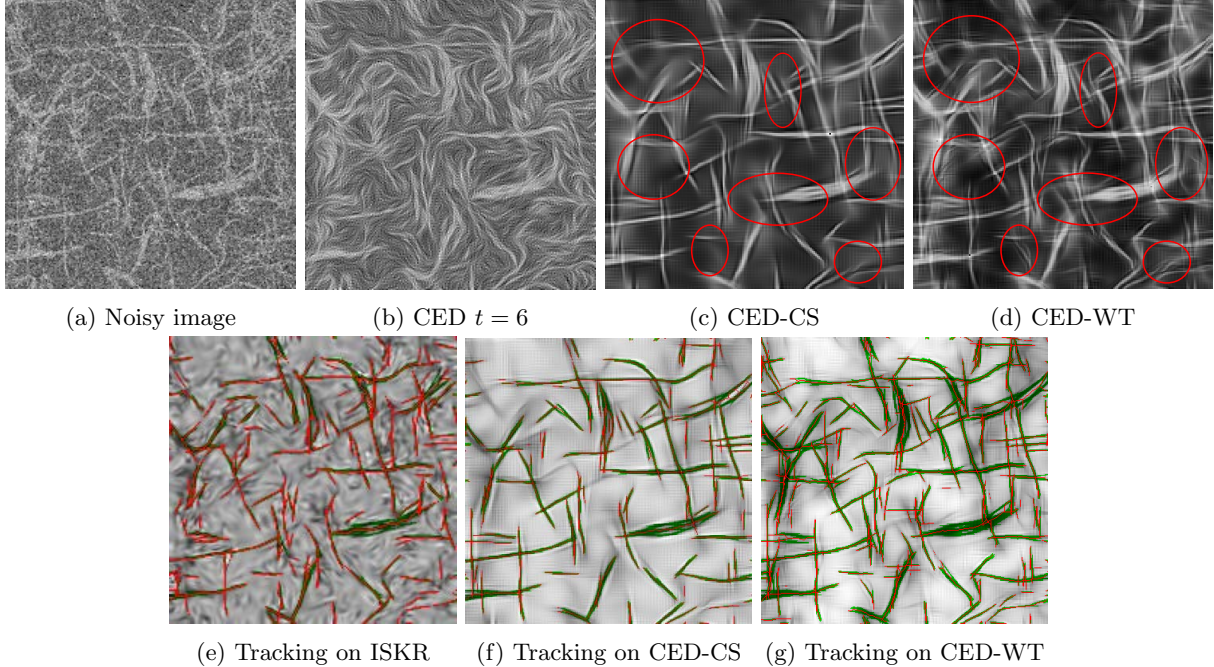


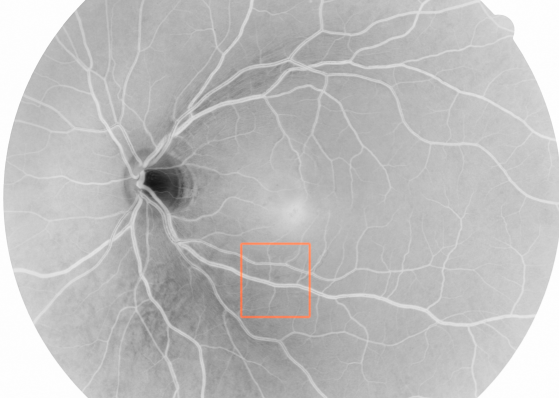
Figure 11: Top: Results of enhancement on an image containing collagen fibres from a bone tissue. (a) Noisy input image (b) CED (c) CED-CS (d) CED-WT ($t_{a_i} = 0, 1, 6, 10$). Circled regions in (c),(d) indicate loss of small-scale information in CED compared CED-WT. (e),(f),(g) show results of a basic line/edge tracking method based [43]. Green indicates line-edges while red indicates centrelines.

CED-CS has the advantage that it is faster and its implementation consumes far less memory (a factor in the order of the number of discrete scales). Tracking on enhancements via ISKR is also presented.

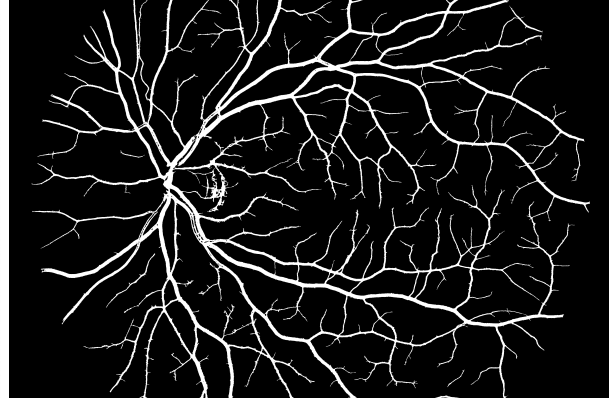
In Figure 12 we show some first results of $SIM(2)$ vesselness-filter described in Section 4.3. These experiments illustrate that the $SIM(2)$ vesselness filter outperforms the multiple scale vesselness filtering acting directly in the image domain, as again no problems arise in areas with crossings/bifurcations. For further underpinning via qualitative and quantitative comparisons on the HRF-benchmark sequence (with manual segmentations by medical professionals) see [60]. In addition to presenting the benefits of our continuous wavelet transform on $SIM(2)$ Figure 12 also shows the potential of including multiple scale crossing-preserving enhancements prior to vesselness filtering (see Figure 12(d) where we have selected a problematic patch). In Figure 13 we show the advantage of using $SIM(2)$ crossing preserving multi-scale enhancements CED-WT prior to tracking retinal vessel via a state of the art tracking algorithm [43].

Table 1: Results in output PSNR (dB) for denoising methods

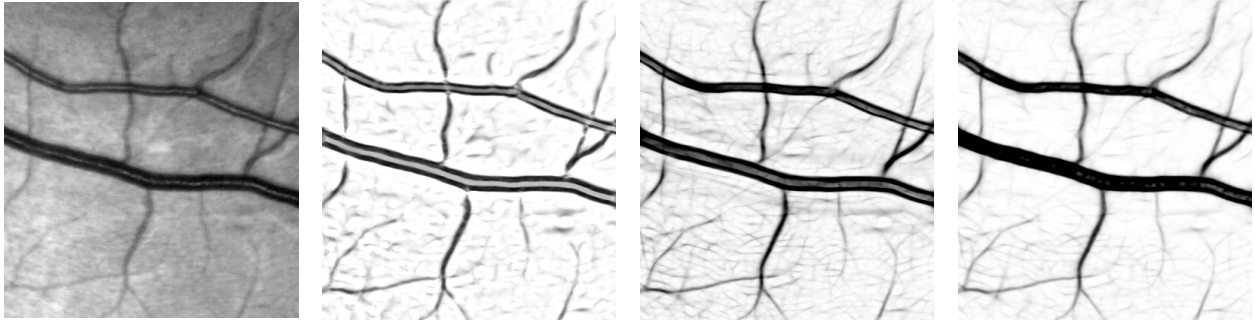
Image	σ /PSNR	NLM	ISKR	BM3D	CED-CS	CED-WT
Bark	30/18.59	21.46	23.85	24.63	21.45	22.02
	50/14.12	20.25	20.89	22.34	20.41	21.34
Lena	40/16.58	25.37	26.20	27.31	23.23	24.68
	50/14.12	24.08	24.23	26.34	23.1	24.12
	60/12.54	22.95	21.17	25.54	21.78	23.16
Collagen Fibrin	20/22.11	26.16	28.26	28.72	25.88	26.17
	30/18.59	22.75	26.41	26.75	25.11	25.31



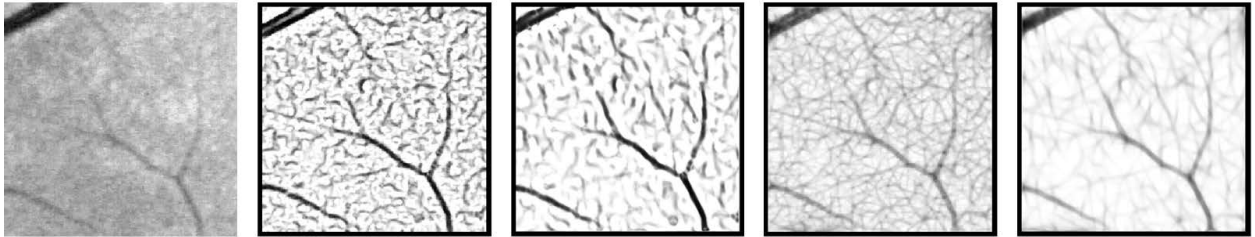
(a) Optical image of the retina where bloodvessels depart from the optic disk



(b) Segmented image via morphological components [60] based on the $SIM(2)$ vesselness filter.



(c) comparison of vesselness filters. Left to Right: fragment of retinal image; Frangi vesselness filter [59] on image; $SIM(2)$ vesselness filter with frame $\partial_\theta, \partial_\xi, \partial_\eta, (\partial_\tau)$; $SIM(2)$ vesselness filter with gauge frame $\partial_a, \partial_b, \partial_c, (\partial_\tau)$, see Eq.(50).



(d) comparison of vesselness filters on a tough retinal image patch with/without enhancements. Left to Right: typical fragment of retinal image where vesselness with standard parameters for the entire image fails; Frangi vesselness filter; Frangi vesselness filter after pre-enhancement via CED-WT; $SIM(2)$ vesselness filter; $SIM(2)$ vesselness filter after pre-enhancement via CED-WT.

Figure 12: Figures (b) shows the result of $SIM(2)$ vesselness (Section 4.3) on an entire retinal fundus image (HRF database). See [60] for details. Figure (c) shows the advantage of $SIM(2)$ vesselness over commonly used Frangi approach. Figure (d) shows the advantage of enhancing the image prior to applying vesselness filters.

In conclusion CED-WT does compete with NLM and ISKR even on noisy images containing only few (multiple-scale crossing) lines. In terms of uncorrelated Gaussian noise reduction via PSNR, BM3D outperforms CED-WT. On noisy medical images with crossing multiple lines our method performs visually better than ISKR and NLM. Compared to BM3D our method has lower performance on large flat areas and a

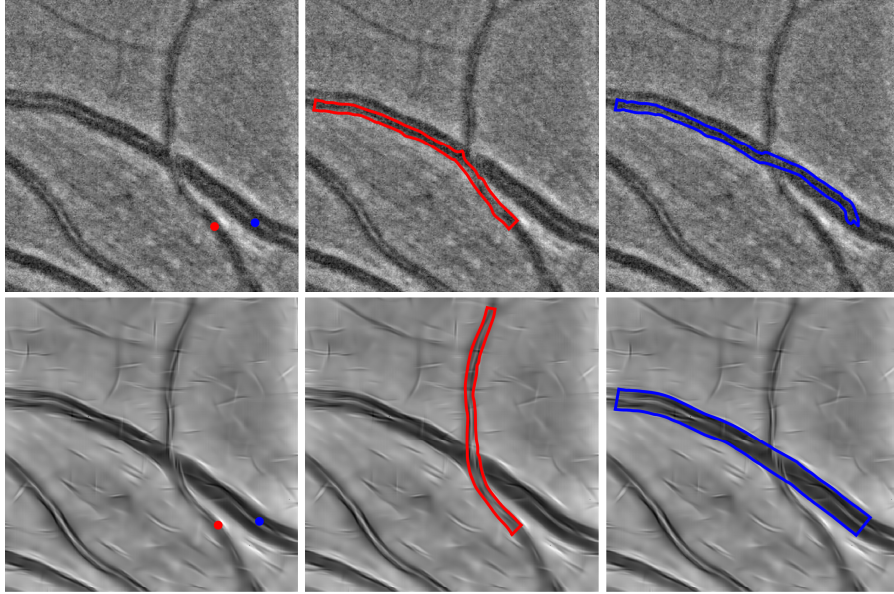


Figure 13: Advantage of $SIM(2)$ crossing preserving multi-scale enhancement in the tracking of retinal vessels via state of the art tracking algorithm [43]. Top: Tracking in the wavelet domain applied to original image data (depicted on the left with seed-points) fails due to noise. Bottom: Tracking in the wavelet domain (where the red/blue tract corresponds to red/blue seed-point) applied after enhancement via CED-WT is successful.

slightly better at multiple scale crossings. Since CED-WT is essentially a diffusion-based method it adds blur to enhancements. This is responsible for lower PSNR values at smaller noise levels. Furthermore in a diffusion process grey-scale intensities dampen and this causes changes in intensity range. Therefore we apply the rescaling approach in Eq.(52). Changing the rescaling approach might increase PSNR values for CED-WT.

By construction CED-WT relies on probabilistic line propagation and makes lines more coherent as visually seen in the experiments. This coherent-line propagation property of CED-WT could be useful as preprocessing for vessel tracking, especially when the tracking takes place in the CS/WT domain [43]. First feasibility experiments presented in Figures 11,12,13 seem to confirm this. However a complete analysis in this direction is beyond the scope of this methodological article and is left to future work. For a comparison of retinal-vessel tracking with segmented ground truth (indicated by medical professionals) based on $SIM(2)$ -vesselness tracking in the wavelet domain see [60].

6. Conclusions

There are two different methodological achievements in this article:

1. Designing an appropriate CW transform on $SIM(2)$, which also allows for accurate and efficient implementation of subsequent enhancement by contextual flows.
2. Construction of contextual flows in the wavelet domain for the enhancement of elongated multi-scale crossing/bifurcating structures, via left-invariant PDEs on $SIM(2)$.

Regarding the first task we have presented a generalized unitarity result for Lie groups which are semi-direct product of group of translations with other Lie groups. This result is then used to design a CW transform appropriate for subsequent left-invariant flows.

For the second task we have shown that only left-invariant flows on the range of $SIM(2)$ -CW transform robustly relate to Euclidean invariant operations on images. Furthermore we have provided a differential-geometric and probabilistic interpretation of left-invariant PDEs on $SIM(2)$ which provides a strong intuitive rationale for the choice of left-invariant PDEs and involved diffusion parameters.

We have also derived analytic approximations of Green's function of linear diffusion on $SIM(2)$. Finally, we have presented crossing multiple-scale (curvature adaptive) flows (CED-WT) via non-linear left-invariant diffusions on the range of $SIM(2)$ -WT transform. Our preliminary results indicate that including the notion of scale indeed has clear advantages over existing PDE techniques (CED, CED-CS). The experiments in the results section show that CED-WT also competes with non-PDE approaches such as NLM and ISKR though BM3D shows better performance than CED-WT (especially at locally flat areas). First feasibility studies indicate that CED-WT due to its multiple scale crossing-preserving coherent line propagation is beneficial prior to (vessel-) tracking, especially if the tracking is performed in the CS/WT domain [43].

An interesting next step would be to include scale interactions, see [66] for motivation, in numerical implementation of non-linear diffusion on $SIM(2)$. Extending and inclusion of the framework of scattering operators on Lie groups (Mallat et al. [52, 53]) to connect scattering operators to PDEs on $SIM(2)$ are interesting topics for future work.

Acknowledgements. The authors would like to thank Erik Bekkers, Jiong Zhang and Julius Hannink for fruitful discussions and various numerical implementations used in this article. The authors also thank the anonymous referees for valuable suggestions and comments. The research leading to the results of this article has received funding from the European Research Council under the European Community's 7th Framework Programme (FP7/2007-2014)/ERC grant agreement No. 335555.



Appendix A. Proof of Theorem 1

For every $\Phi \in \mathbb{C}_K^G$ has a \mathcal{W}_ψ pre-image $f \in \mathbb{L}_2(\mathbb{R}^d)$, i.e. $f = (\mathcal{W}_\psi)^{-1}[\Phi]$ with $\|\Phi\|_{\mathbb{C}_K^G}^2 = (\Phi, \Phi)_{\mathbb{C}_K^G} = (f, f)_{\mathbb{L}_2(\mathbb{R}^d)} = \|f\|_{\mathbb{L}_2(\mathbb{R}^d)}^2$. We need to show that $\|\Phi\|_{\mathbb{C}_K^G}^2 = \|\Phi\|_{M_\psi}^2 := (\Phi, \Phi)_{M_\psi}^{\frac{1}{2}}$, where we recall (4) for the definition of the M_ψ -inner product. We have,

$$\int_{\mathbb{R}^d} |f(y)|^2 dy = \int_{\mathbb{R}^d} |\hat{f}(\omega)|^2 d\omega = \int_{\bar{\Omega}} |\hat{f}(\omega)|^2 \frac{M_\psi(\omega)}{M_\psi(\omega)} d\omega = \int_{\Omega} |\hat{f}(\omega)|^2 \frac{M_\psi(\omega)}{M_\psi(\omega)} d\omega. \quad (\text{A.1})$$

Recall that T is assumed to be a linear algebraic group (see [42] for definition) and therefore it has locally closed (dual) orbits. This leads to $\Omega_c = \Omega_{cr}$ in [36, Ch 5] and since Ω_{cr} is open, [36, Prop 5.7], we have that $\mu(\bar{\Omega} \setminus \Omega) = 0$, where μ is the usual Lebesgue measure on \mathbb{R}^d , giving us the final equality in (A.1). We can further write (A.1) as,

$$\begin{aligned} \int_{\mathbb{R}^d} |f(y)|^2 dy &= \int_{\Omega} |\hat{f}(\omega)|^2 \frac{1}{M_\psi(\omega)} \int_T \frac{|\mathcal{FR}_t \psi(\omega)|^2}{\det(\tau(t))} d\mu_T(t) d\omega = \int_{\Omega} \left\{ \int_T \frac{\overline{\hat{f}(\omega)} (\mathcal{FR}_t \psi(\omega)) \hat{f}(\omega) (\mathcal{FR}_t \psi(\omega))}{\det(\tau(t))} \right\} \frac{d\omega}{M_\psi(\omega)} \\ &= \int_{\Omega} \int_T \overline{(\mathcal{F}\Phi(\cdot, t))(\omega)} (\mathcal{F}\Phi(\cdot, t))(\omega) d\mu_T(t) \frac{d\omega}{M_\psi(\omega)} = \int_{\Omega} \left(\int_T |\mathcal{F}\Phi(\cdot, t)(\omega)|^2 d\mu_T(t) \right) M_\psi^{-1}(\omega) d\omega. \end{aligned}$$

As a result $\Phi \in \mathbb{H}_\psi \otimes \mathbb{L}_2(T; \frac{d\mu_T(t)}{det(\tau(t))})$ and we obtain

$$(f, f)_{\mathbb{L}_2(\mathbb{R}^d)} = (\mathcal{W}_\psi f, \mathcal{W}_\psi f)_{\mathbb{C}_K^G} = \int_T \left(M_\psi^{-\frac{1}{2}} \mathcal{F}\Phi(\cdot, t), M_\psi^{-\frac{1}{2}} \mathcal{F}\Phi(\cdot, t) \right) d\mu_T(t).$$

Appendix B. Explicit formulation of exponential and logarithm curves

The exponential curves $g_0\gamma_c(t) = (x(t), y(t), \tau(t), \theta(t))$ passing through $g_0 = (x_0, y_0, e^{\tau_0}, \theta_0)$ at $t = 0$ is,

$$\begin{aligned} x(t) &= \frac{1}{c_1^2 + c_4^2} [e^{\tau_0} c_1 ((-\sin[\theta_0] + e^{tc_4} \sin[tc_1 + \theta_0]) c_2 + (-\cos[\theta_0] + e^{tc_4} \cos[tc_1 + \theta_0]) c_3) + c_1^2 x_0 + \\ &\quad c_4 (e^{\tau_0} (-\cos[\theta_0] + e^{tc_4} \cos[tc_1 + \theta_0]) c_2 + e^{\tau_0} (\sin[\theta_0] - e^{tc_4} \sin[tc_1 + \theta_0]) c_3 + c_4 x_0)] \\ y(t) &= \frac{1}{c_1^2 + c_4^2} [e^{\tau_0} c_1 ((\cos[\theta_0] - e^{tc_4} \cos[tc_1 + \theta_0]) c_2 + (-\sin[\theta_0] + e^{tc_4} \sin[tc_1 + \theta_0]) c_3) + c_1^2 y_0 + \\ &\quad c_4 (e^{\tau_0} (-\sin[\theta_0] + e^{tc_4} \sin[tc_1 + \theta_0]) c_2 + e^{\tau_0} (-\cos[\theta_0] + e^{tc_4} \cos[tc_1 + \theta_0]) c_3 + c_4 y_0)] \\ \tau(t) &= tc_4 + \tau_0, \quad \theta(t) = tc_1 + \theta_0. \end{aligned} \tag{B.1}$$

To explicitly determine the log map, we solve for $\{c^1, c^2, c^3, c^4\}$ from equality, $g = \exp\left(t \sum_{i=1}^4 c^i A_i\right)$, yielding

$$c^1 = \theta/t, \quad c^2 = \frac{(y\theta - x\tau) + (-\theta\eta + \tau\xi)}{t(1 + e^{2\tau} - 2e^\tau \cos\theta)}, \quad c^3 = \frac{-(x\theta + y\tau) + (\theta\xi + \tau\eta)}{t(1 + e^{2\tau} - 2e^\tau \cos\theta)}, \quad c^4 = \tau/t, \tag{B.2}$$

where we have made use of the definition $\xi = e^\tau(x \cos\theta + y \sin\theta)$ and $\eta = e^\tau(-x \sin\theta + y \cos\theta)$.

References

- [1] T. Lindeberg, Scale-Space Theory in Computer Vision, Kluwer international series in engineering and computer science: Robotics: Vision, manipulation and sensors, Springer, 1993.
- [2] L. Alvarez, F. Guichard, P.-L. Lions, J.-M. Morel, Axioms and fundamental equations of image processing, Archive for rational mechanics and analysis 123 (3) (1993) 199–257.
- [3] B. ter Haar Romeny, L. Florack, J. Koenderink, M. Viergever, Scale-Space Theory in Computer Vision: First International Conference, Scale-Space'97, Utrecht, The Netherlands, July 2-4, 1997, Proceedings, Vol. 1252, Springer, 1997.
- [4] T. Lindeberg, Generalized axiomatic scale-space theory, in: Advances in Imaging and Electron Physics, Vol 178, Advances in Imaging and Electron Physics, Elsevier, 2013, pp. 1–96.
- [5] P. Perona, J. Malik, Scale-space and edge detection using anisotropic diffusion, Pattern Analysis and Machine Intelligence, IEEE Transactions on 12 (7) (1990) 629–639. doi:10.1109/34.56205.
- [6] J. Weickert, Coherence-enhancing diffusion filtering, International Journal of Computer Vision 31 (2-3) (1999) 111–127.
- [7] E. Franken, R. Duits, Crossing-preserving coherence-enhancing diffusion on invertible orientation scores, International Journal of Computer Vision 85 (2009) 253–278.
- [8] H. Scharr, K. Krajsek, A short introduction to diffusion-like methods, in: Mathematical methods for signal and image analysis and representation, Computational imaging and vision, Springer London, 2012, Ch. 1.
- [9] L. Florack, Image Structure, Kluwer Academic Publishers, Dordrecht, The Netherlands, 1997.
- [10] R. Duits, B. Burgeth, Scale spaces on lie groups, in: Proceedings of the 1st international conference on Scale space and variational methods in computer vision, SSVM'07, Springer-Verlag, Berlin, Heidelberg, 2007, pp. 300–312.

- [11] G. Citti, A. Sarti, A cortical based model of perceptual completion in the roto-translation space, *Journal of Mathematical Imaging and Vision* 24 (3) (2006) 307–326.
- [12] R. Duits, H. Führ, B. Janssen, M. Bruurmijn, L. Florack, H. van Assen, Evolution equations on gabor transforms and their applications, *Applied and Computational Harmonic Analysis* 35 (2013) 483–526.
- [13] R. Duits, Perceptual Organization in Image Analysis, Ph.D. thesis, Technische Universiteit Eindhoven (2005). URL <http://bmia.bmt.tue.nl/people/RDuits/THESISRDUIITS.pdf>
- [14] G. C. DeAngelis, I. Ohzawa, R. D. Freeman, Receptive-field dynamics in the central visual pathways, *Trends in Neurosciences* 18 (10) (1995) 451–458.
- [15] R. Young, The gaussian derivative model for spatial vision: I. retinal mechanisms, *Spatial Vision* 2 (4) (1987) 273–293.
- [16] M. Landy, J. Movshon, Computational models of visual processing, Bradford book, Mit Press, 1991.
- [17] W. Bosking, Y. Zhang, B. Schofield, D. Fitzpatrick, Orientation selectivity and the arrangement of horizontal connections in tree shrew striate cortex, *The Journal of Neuroscience* 17(6) (1997) 2112–2127.
- [18] R. Duits, M. Felsberg, G. Granlund, B. ter Haar Romeny, Image analysis and reconstruction using a wavelet transform constructed from a reducible representation of the Euclidian motion group, *Int. J. Comput. Vision* 72 (1) (2007) 79–102.
- [19] J.-P. Antoine, R. Murenzi, Two-dimensional directional wavelets and the scale-angle representation, *Signal Processing* 52 (3) (1996) 259–281.
- [20] J.-P. Antoine, R. Murenzi, P. Vandergheynst, Directional wavelets revisited: Cauchy wavelets and symmetry detection in patterns, *Applied and Computational Harmonic Analysis* 6 (3) (1999) 314–345.
- [21] J.-P. Antoine, R. Murenzi, P. Vandergheynst, S. Ali, Two-dimensional wavelets and their relatives, Cambridge University Press, 2004.
- [22] L. Jacques, L. Duval, C. Chaux, G. Peyré, A panorama on multiscale geometric representations, intertwining spatial, directional and frequency selectivity, *Signal Processing* 91 (12) (2011) 2699–2730.
- [23] S. T. Ali, J.-P. Antoine, J.-P. Gazeau, Coherent States, Wavelets, and Their Generalizations, Springer New York, 2014.
- [24] D. Donoho, E. Candès, Ridgelets: a key to higher-dimensional intermittency?, *Royal Society of London Philosophical Transactions Series A* 357 (1999) 2495–2509.
- [25] D. Donoho, E. Candès, Continuous curvelet transform: I. resolution of the wavefront set, *Applied and Computational Harmonic Analysis* 19 (2) (2005) 162–197.
- [26] D. Donoho, E. Candès, Continuous curvelet transform: II. discretization and frames, *Applied and Computational Harmonic Analysis* 19 (2) (2005) 198–222.
- [27] E. Candès, L. Demanet, D. Donoho, L. Ying, Fast discrete curvelet transforms, *Multiscale Modeling and Simulation* 5 (2006) 861–899.
- [28] D. Labate, W.-Q. Lim, G. Kutyniok, G. Weiss, Sparse multidimensional representation using shearlets, in: *Optics & Photonics 2005*, International Society for Optics and Photonics, 2005, pp. 59140U–59140U.
- [29] K. Guo, D. Labate, Optimally sparse multidimensional representation using shearlets, *SIAM journal on mathematical analysis* 39 (1) (2007) 298–318.
- [30] S. Dahlke, G. Steidl, G. Teschke, Shearlet coorbit spaces: compactly supported analyzing shearlets, traces and embeddings, *Journal of Fourier Analysis and Applications* 17 (6) (2011) 1232–1255.
- [31] B. G. Bodmann, G. Kutyniok, X. Zhuang, Gabor shearlets, arXiv preprint (arXiv:1303.6556) (2013).

- [32] U. Sharma, R. Duits, Left-invariant evolutions of wavelet transforms on the similitude group, arXiv preprint (2014).
URL <http://arxiv.org/abs/1306.1800>
- [33] S. T. Ali, A general theorem on square-integrability: Vector coherent states, *J. Math. Phys.* 39(8) (1998) 3954–3964.
- [34] D. H. Hubel, Evolution of ideas on the primary visual cortex, 1955-1978: A biased historical account, *Physiology or Medicine Literature Peace Economic Sciences, Nobel Prize Lectures* (1993) 24.
- [35] A. Grossmann, J. Morlet, T. Paul, Transforms associated to square integrable group representations. I. General results, *J. Math. Phys.* 26 (10) (1985) 2473–2479.
- [36] H. Führ, *Abstract Harmonic Analysis of Continuous Wavelet Transforms*, no. 1863 in *Lecture Notes in Mathematics*, Springer, 2005.
- [37] S. Kalitzin, B. ter Haar Romeny, M. Viergever, Invertible apertured orientation filters in image analysis, *International Journal of Computer Vision* 31 (2-3) (1999) 145–158.
- [38] R. Duits, M. Almsick, The explicit solutions of linear left-invariant second order stochastic evolution equations on the 2D Euclidean motion group, *Quarterly of Applied Mathematics* 66 (2008) 27–67.
- [39] R. Duits, E. Franken, Left-invariant parabolic evolutions on $SE(2)$ and contour enhancement via invertible orientation scores part I: Linear left-invariant diffusion equations on $SE(2)$, *Quarterly of Applied Mathematics* 68 (2010) 255–292.
- [40] R. Duits, E. Franken, Left-invariant parabolic evolutions on $SE(2)$ and contour enhancement via invertible orientation scores part II: Nonlinear left-invariant diffusions on invertible orientation scores, *Quarterly of Applied Mathematics* 68 (2010) 293–331.
- [41] F. Martens, Spaces of analytic functions on inductive/projective limits of Hilbert Spaces, Ph.D. thesis, Technische Universiteit Eindhoven (1988).
URL <http://alexandria.tue.nl/extra3/proefschrift/PRF6A/8810117.pdf>
- [42] A. Borel, H. Bass, *Linear algebraic groups*, Vol. 126, Springer-Verlag New York, 1991.
- [43] E. Bekkers, R. Duits, T. Berendschot, B. ter Haar Romeny, A multi-orientation analysis approach to retinal vessel tracking, *Journal of Mathematical Imaging and Vision* (2012) 1–28.
- [44] U. Boscaïn, J.-P. Gauthier, R. Chertovskih, A. Remizov, Hypoelliptic diffusion and human vision, arXiv preprint (arXiv:1304.2062) (2013).
- [45] L. Jacques, J.-P. Antoine, Multiselective pyramidal decomposition of images: wavelets with adaptive angular selectivity, *International Journal of Wavelets, Multiresolution and Information Processing* 5 (05) (2007) 785–814.
- [46] J. Dieudonné, *Treatise on Analysis*, no. v. 5 in *Pure and applied mathematics*, Academic Press, 1977.
- [47] E. Franken, Enhancement of crossing elongated structures in images, Ph.D. thesis, Technische Universiteit Eindhoven (2008).
URL <http://alexandria.tue.nl/extra2/200910002.pdf>
- [48] L. Hörmander, Hypoelliptic second order differential equations, *Acta Mathematica* 119 (1967) 147–171.
- [49] E. Hsu, *Stochastic analysis on manifolds*, *Contemporary Mathematics*, American Mathematical Society, 2002.
- [50] A. Nagel, F. Ricci, E. M. Stein, Fundamental solutions and harmonic analysis on nilpotent groups, *Bulletin of American Mathematical Society* 23 (1990) 139–144.
- [51] A. ter Elst, D. Robinson, Weighted subcoercive operators on Lie groups, *Journal of Functional Analysis* 157 (1) (1998) 88–163.

- [52] S. Mallat, Group invariant scattering, *Communications on Pure and Applied Mathematics* 65 (10) (2012) 1331–1398.
- [53] L. Sifre, S. Mallat, Rotation, scaling and deformation invariant scattering for texture discrimination, in: *Computer Vision and Pattern Recognition (CVPR)*, 2013, pp. 1233–1240.
- [54] N. Patton, T. M. Aslam, T. MacGillivray, I. J. Deary, B. Dhillon, R. H. Eikelboom, K. Yogesan, I. J. Constable, Retinal image analysis: concepts, applications and potential, *Progress in retinal and eye research* 25 (1) (2006) 99–127.
- [55] A. Budai, J. Hornegger, G. Michelson, Multiscale approach for blood vessel segmentation on retinal fundus images, *Investigative Ophthalmology and Visual Science* 50 (5) (2009) 325.
- [56] M. D. Abràmoff, M. K. Garvin, M. Sonka, Retinal imaging and image analysis, *Biomedical Engineering, IEEE Reviews in* 3 (2010) 169–208.
- [57] X. Xu, M. Niemeijer, Q. Song, M. Sonka, M. K. Garvin, J. M. Reinhardt, M. D. Abràmoff, Vessel boundary delineation on fundus images using graph-based approach, *Medical Imaging, IEEE Transactions on* 30 (6) (2011) 1184–1191.
- [58] P. Bankhead, C. N. Scholfield, J. G. McGeown, T. M. Curtis, Fast retinal vessel detection and measurement using wavelets and edge location refinement, *PloS one* 7 (3) (2012) e32435.
- [59] A. F. Frangi, W. J. Niessen, K. L. Vincken, M. A. Viergever, Multiscale vessel enhancement filtering, in: *Medical Image Computing and Computer-Assisted Intervention MICCAI'98*, Springer, 1998, pp. 130–137.
- [60] J. Hannink, R. Duits, E. Bekkers, Vesselness via multiple scale orientation scores, *arXiv preprint* (2014).
URL <http://arxiv.org/abs/1402.4963>
- [61] A. Buades, B. Coll, J.-M. Morel, A review of image denoising algorithms, with a new one, *Multiscale Modeling & Simulation* 4 (2) (2005) 490–530, Implementation: *Mathematica* 9.
- [62] H. Takeda, S. Farsiu, P. Milanfar, Kernel regression for image processing and reconstruction, *Image Processing, IEEE Transactions on* 16 (2) (2007) 349–366.
URL Implementation: <http://users.soe.ucsc.edu/~htakeda/kernelreg/kernelreg.htm>
- [63] M. Lebrun, An Analysis and Implementation of the BM3D Image Denoising Method, *Image Processing On Line* 2 (2012) 175–213.
- [64] K. Dabov, A. Foi, V. Katkovnik, K. Egiazarian, Image denoising by sparse 3-d transform-domain collaborative filtering, *Image Processing, IEEE Transactions on* 16 (8) (2007) 2080–2095.
URL Implementation: <http://www.cs.tut.fi/~foi/GCF-BM3D/>
- [65] M. Rubbens, A. Mol, R. Boerboom, R. Bank, F. Baaijens, C. Bouten, Intermittent straining accelerates the development of tissue properties in engineered heart valve tissue, *Tissue Engineering: Part A* 15 (5).
- [66] A. Sarti, G. Citti, J. Petitot, The symplectic structure of the primary visual cortex, *Biological Cybernetics* 98 (1) (2008) 33–48.